Cerium–Copper–Manganese Oxides Synthesized via Solution Combustion Synthesis (SCS) for Total Oxidation of VOCs

(Article begins on next page)

26 April 2024

# Cerium–Copper–Manganese Oxides Synthesized via Solution Combustion Synthesis (SCS) for Total Oxidation of VOCs

Miguel Jose Marin Figueredo[1] · Tahrizi Andana[1] · Samir Bensaid[1] · Melodj Dosa[1] · Debora Fino[1] · Nunzio Russo[1] · Marco Piumetti[1]

Abstract

A set of cerium–manganese–copper oxide catalysts with various foreign metal contents was prepared via the solution combustion synthesis (SCS). The catalysts were characterized by complementary techniques such as N_2 physisorption at -196 °C, X-ray diffraction (XRD), field-emission scanning electron microscopy (FESEM), H_2-temperature-programmed reduction (H_2-TPR), O_2-temperature-programmed desorption (O_2-TPD) and X-ray photoelectron spectroscopy (XPS). Their catalytic activity was tested towards the VOC oxidation using ethylene and propylene as probe molecules. As a whole, it has been observed that the $Ce_{55}Mn_{45}$ sample (Mn 45 at.%), containing MnO_x clusters interacting with the ceria phase, was the most active catalyst for propylene oxidation, exhibiting a complete conversion at 250 °C. On the other hand, the ternary oxide catalyst ($Ce_{55}Mn_{22.5}Cu_{22.5}$ with Mn = 22.5 at.% and Cu = 22.5 at.%) has exhibited the best results for the oxidation of ethylene. These findings suggest that the co-presence of different active phases on the catalytic surface may have a beneficial (multiplicative) role on the whole reactivity. Finally, the most active powder catalysts were wash-coated in a SiC monolith and tested in a bench-scale reactor. As a whole, the catalyzed monoliths performed the complete oxidation of either ethylene or propylene at lower temperatures (550 and 450 °C, respectively) than those required to thermally decompose these molecules.

Graphic Abstract
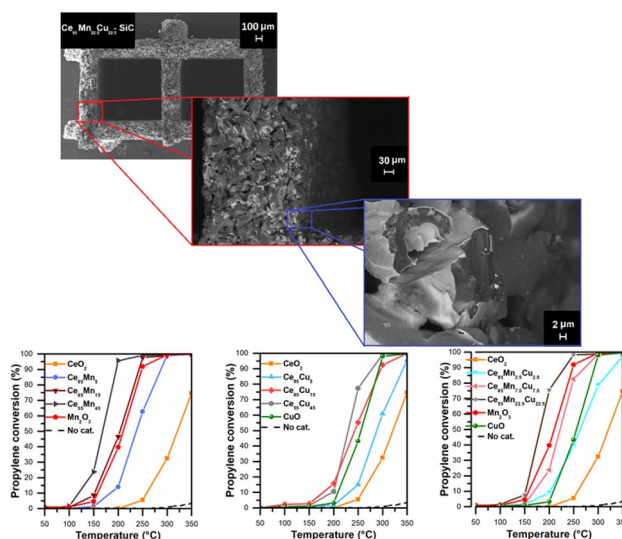
Extended author information available on the last page of the article

1 Introduction

Volatile organic compounds (VOCs) include any organic substance having a boiling point equal or lower than 250 °C at standard pressure (i.e. 101.3 kPa). In EU as well as in several other countries in the world, there are already regulations and control of substances effectively classified as VOCs and their production at industrial level [1, 2]. These substances may derive from two different sources: biogenic, if they are produced in several processes occurring between the Earth's crust and the atmosphere, or anthropogenic, if they result from human-related activities [3]. A virtually inevitable production of VOCs comes from household activities (e.g. cleaning, painting) or from various industrial activities where chemical and/or physical processes are performed, such as automotive, petrochemical, waste management and food processing [3]. When humans are exposed to VOCs, these compounds have demonstrated to represent a toxic, carcinogenic, mutagenic or teratogenic risk [4], which motivated further observations on airborne chemical contact in indoor environments [5, 6].

In this context, several abatement techniques have been developed to diminish the emissions of VOCs such as thermal or catalytic oxidation, adsorption, absorption and condensation [7]. Catalytic oxidation has demonstrated to be a suitable technique to perform an effective abatement of pollutants in gaseous streams containing variable flow rates and concentrations [8]. Some examples of the abated pollutants could be different hydrocarbons and diesel soot [9–11]. The latter can be oxidized through different mechanisms or kinetics depending on different factors (e.g. operating conditions, catalyst, reactants, etc.). The kinetic models that describe the VOCs oxidation over oxide catalysts typically involve the Langmuir–Hinshelwood and/or the Mars–van Krevelen-type mechanisms [9]. Different materials have shown promising performances in the catalytic oxidation of VOCs under various reaction conditions. Such materials can be supported noble metals (e.g. Pd, Pt, Ag and Au), which have shown to be active at low temperatures [9, 12]. Non-noble metal oxides like oxides of manganese, copper and cerium have also been widely studied. They are cheaper and more resistant to chemical poisoning than the noble metals as well as they can be active at relatively high temperatures [9, 12]. Mixed oxides have also shown to be active in the oxidation of several VOCs, due to possible synergies among the oxide phases in the catalyst [13–16].

Cerium (IV) oxide has demonstrated its efficacy in catalysis due to its redox properties and oxygen storage capacity, as well as it is able to endorse Mars–Van Krevelen

(MvK)-type mechanisms [9, 16, 17]. Since the MvK mechanism occurs through oxygen species from the solid, the "redox-flexibility" of the material becomes a key factor for the catalytic oxidation reaction. Thus, both the electronic and structural changes caused by the introduction of foreign metals in the ceria lattice seem to be beneficial toward the VOC oxidation reactions.

It appears that doping leads to improvements in terms of structural stability, oxygen storage capacity and mobility. Moreover, the surface reducibility of ceria-based catalysts can be improved via the presence of two or more oxide phases (e.g. CeO_2 with MnO_x, CuO_x) interacting with each other thus inducing the formation of oxygen vacancies [17–22].

In the present work, three sets of mixed oxide catalysts, two binary oxides (Ce–Mn and Ce–Cu) and one ternary oxide (Ce–Mn–Cu), with various foreign metal loadings were synthesized via solution combustion synthesis (SCS). The catalysts were characterized by the N_2 physisorption at −196 °C, X-ray diffraction analysis, X-ray photoelectron spectroscopy, H_2 temperature-programmed reduction, O_2 temperature-programmed desorption and field emission scanning electronic microscopy. Their catalytic activity was tested towards VOC oxidation reactions, using ethylene and propylene as probe molecules. Indeed, the two hydrocarbons are representative of a wide group of VOCs and therefore possible precursors of carbonaceous matter.

The most active powder catalysts were then deposited on a silicon carbide (SiC)-based monolith via a novel in-situ SCS. The catalyzed monoliths were finally tested for the VOC oxidation in a bench-scale reactor.

2 Experimental

2.1 Catalysts Preparation

Pure cerium, manganese and copper oxides, as well as binary (Ce–Mn, Ce–Cu) and ternary oxide catalysts (Ce–Mn–Cu) were prepared through the solution combustion synthesis (SCS) [13, 19, 23–25]. The mixed oxide catalysts were prepared with different foreign metal contents: 5, 15 and 45 at.%. The notation is: $Ce_{100−x}M_x$, where M represents either Mn or Cu for the binary oxides, and $Ce_{100−x}Mn_{x/2}Cu_{x/2}$ for the ternary oxides. Therefore, the list of powder catalysts prepared in the current work is: CeO_2, $Ce_{95}Mn_5$, $Ce_{85}Mn_{15}$, $Ce_{55}Mn_{45}$, Mn_2O_3, $Ce_{95}Cu_5$, $Ce_{85}Cu_{15}$, $Ce_{55}Cu_{45}$, CuO, $Ce_{95}Mn_{2.5}Cu_{2.5}$, $Ce_{85}Mn_{7.5}Cu_{7.5}$, $Ce_{55}Mn_{22.5}Cu_{22.5}$. During a typical synthesis, proper amounts of metal precursors,

namely $Ce(NO_3)_3 \cdot 6H_2O$ (Alfa Aesar); $Mn(NO_3)_2 \cdot 4H_2O$; $Cu(NO_3)_2 \cdot 3H_2O$ (Sigma-Aldrich), were dissolved in 100 ml of deionized water along with a "fuel" (urea), whose amount was made in excess (200% of the stoichiometric amount). The amounts of precursors were defined to have nominal metal-to-cerium ratios.

The mixture was stirred vigorously at r.t. for 5 min. Then, the homogeneous aqueous solution was heated in oven at 650 °C for 30 min.

The most catalytically active powder samples (namely, $Ce_{55}Mn_{22.5}Cu_{22.5}$ and $Ce_{55}Mn_{45}$) were washcoated in silicon carbide (SiC) monoliths [Céramiques Techniques et Industrielles s.a.s., 290 cpsi (cells per square inch), 3 cm in length and 2.54 cm in diameter], through an in-situ SCS with the same precursor mixtures used for the preparation of powder catalysts. The deposition was carried out by carefully injecting the precursor solution to the inner channels of the SiC monolith. Then, the monolith was placed in a preheated oven at a calcination temperature of 650 °C for 5 min. After a fast synthesis/calcination, the monolith was cooled down till r.t. and subsequently blown with compressed air to remove the undeposited powder from the channels. This procedure was repeated several times till the catalyst loading was equivalent to 15 wt%. The two monoliths are denoted as $Ce_{55}Mn_{45}$–SiC and $Ce_{55}Mn_{22.5}Cu_{22.5}$–SiC.

2.2 Catalyst Characterization

The X-ray diffraction (XRD) patterns were measured on a X'Pert Philips PW3040 diffractometer using a Cu K_α radiation (2θ range 20° to 80°, step = 0.05° 2θ, time per step = 0.2 s). Such patterns were analyzed using the Powder Data File Database (PDF 2000, International Centre of Diffraction Data, Pennsylvania). The average size of the crystallites was determined through the use of the Scherrer formula, $D = 0.9\lambda/(b \cos \theta)$, where λ is the wavelength of the Cu K_α radiation, b is the full width at half maximum (in radians), 0.9 is the shape factor considered for spherical particles and θ is the angle of the diffraction peaks.

The specific surface area (S_{BET}), total pore volume (V_P) and the average pore diameter (D_P) were determined through the N_2 physisorption analysis at − 196 °C (Micromeritics Tristar II 3020) on powders previously outgassed at 200 °C for 2 h to remove moisture/adsorbed water and atmospheric pollutants. The S_{BET} was determined according to the Brunauer, Emmett and Teller (BET) method.

The catalyst morphology was studied through a field emission scanning electronic microscope (FESEM) Zeiss Merlin, Gemini-II column, using an extra high tension (EHT) of 3 kV, a working distance (WD) of 2.8 mm and a probe intensity of 120 pA. Additionally, the chemical composition of the catalysts was determined through EDS analysis (Oxford X-ACT) on two different areas/zones on

the sample with a size/diameter of 5–25 μm. To analyze the distribution of different elements on the surface of the samples, EDS color coded mapping was also performed for the most active catalysts.

Temperature-programmed reduction/desorption analysis was realized in a ThermoQuest TPD/R/O 1100 analyzer, equipped with a thermal conductivity detector (TCD). The reducibility of the powder catalysts was studied by H_2-TPR, in which a pretreatment was carried out before the analysis by treating 50 mg of the sample with helium (40 ml min^{-1}) at 550 °C for 1 h. In the H_2-TPR analysis, the catalyst was placed in a quartz tubular reactor and exposed to a reducing gas flow of 5 vol.% H_2 in Ar (20 ml min^{-1}). The analysis was conducted under a programmed heating from 50 to 800 °C with a ramp of 5 °C min^{-1} and the final temperature hold for 10 min. In the O_2-TPD analysis, 50 mg of sample was initially pretreated under a pure O_2 flow (40 ml min^{-1}) at 550 °C for 30 min and then cooled down to 50 °C still under the O_2 flow. Then, the TPD measurement was performed by heating the sample until 950 °C under a He flow (20 ml min^{-1}) at a constant heating rate (5 °C min^{-1}). For comparison purposes, three commercial MnO_x samples (MnO_2, Mn_2O_3 and MnO, from Sigma-Aldrich) were investigated under the same operating conditions.

XPS (X-ray photoelectron spectroscopy) measurements were performed on an XPS PHI 5000 Versa probe apparatus using the following conditions: band-pass energy of 187.85 eV, a 45° take off angle and a 100.0 μm diameter X-ray spot size. The curve-fitting was performed by means of Multipack 9.0 software.

2.3 Catalytic Activity Tests

Catalytic activity tests of powder samples were performed in a classical temperature-programmed oxidation setup, comprising a fixed-bed quartz U-tube reactor (ID = 4 mm) to host the catalyst powder. The reactor was heated by a PID-controlled furnace and the reactor bed temperature was measured by a K-type thermocouple.

Before the test, 0.1 g of powder catalyst was pretreated to remove the adsorbed species. During the pretreatment, He was fed (flow rate = 15 ml min^{-1}) for 1 h, maintaining a constant temperature of 150 °C. The catalytic test started with feeding to the reactor a gaseous reactive mixture containing 500 ppm of VOC (either ethylene or propylene) and 10 vol.% of O_2 (with N_2 to balance).

During the test, a gas hourly space velocity (GHSV) of 20,000 h^{-1} and a catalyst weight-to-volumetric flow rate ratio (W/F) of 0.065 g h l^{-1} was maintained. The temperature was raised in the range of 50–350 °C, and an isothermal step was performed every 50 °C. The outlet gas composition was measured by using non-dispersive infrared (NDIR) analyzers (ABB Uras 14). To confirm

the reproducibility of the catalytic tests, three consecutive catalytic tests were performed, keeping the same operative conditions. In order to perform the catalytic tests under wet conditions (RH 100%), the reactant gas flow was saturated by bubbling it inside a vessel containing water at 20 °C before flowing it to the U-tube reactor.

To test the activity of the catalytic monoliths ($Ce_{55}Mn_{45}$–SiC and $Ce_{55}Mn_{22.5}Cu_{22.5}$–SiC), a stainless-steel reactor and a horizontal furnace (60 cm-long) were used. To optimize the gas flow distribution in the monolith, the prepared monolith was fixed in a hollowed cordierite monolith (3.5 cm in diameter). The temperatures (inlet and outlet) of the catalyzed monolith were measured by two K-type thermocouples. Before the tests, the monolith was outgassed with He (flow-rate = 300 ml min^{-1}) at 150 °C for 1 h. Then, a gas mixture containing 500 ppm of VOC (either ethylene or propylene) and 10 vol.% of O_2 (with N_2 to balance), was fed to the reactor by mass-flow controllers. GHSV = 9000 h^{-1} and W/F = 0.031 g h l^{-1} were maintained during the tests; the temperature was raised from 100 to 620 °C at a heating rate of 5 °C min^{-1}. The outlet gas composition was then measured by the NDIR. Each test was repeated twice to evaluate the reproducibility. Additionally, time on stream (TOS) tests were performed to study the stability of the catalyzed monolith.

3 Results and Discussion

3.1 Material Textural Properties

In Fig. 1, the XRD patterns of the synthesized catalysts are shown. For pure ceria, the diffraction peaks correspond to the fluorite structure of cerium (IV) oxide (reference code 01-081-0792), with a face-centered-cubic-structure containing octahedral and hexahedral holes filled with oxygen ions [17]. It can be seen that for the binary (Ce–Mn; Ce–Cu) and ternary (Ce–Mn–Cu) oxide catalysts, the most intense peaks corresponding to ceria fluorite structure are still observed for the samples even with a high content of manganese and/or copper. However, in the diffractograms of the binary and ternary oxides with 45% metal content were observed the peaks corresponding to pure oxides of copper or manganese (CuO ref. code 00-045-0937; Mn_2O_3 ref. code 01-078-0390) and mixed copper-manganese oxide ($Cu_{1.5}Mn_{1.5}O_4$ ref. code 01-070-0260), thus suggesting the presence of extra-framework species (metal oxides) from the lattice. It can also be seen that the XRD peak broadens as the metal content increases. This behavior seems related to the fact that the content of small and defect-rich crystallites in the samples is increased [26]. The latter condition, indeed, could favor the formation of smaller crystallites, with an average size of 12 nm (estimated via the Scherrer's formula). This means that elevated percentages of foreign metals in the solids lead to smaller crystallites, as shown the Fig. S1. On the other hand, strain effects along with structural defects could occur
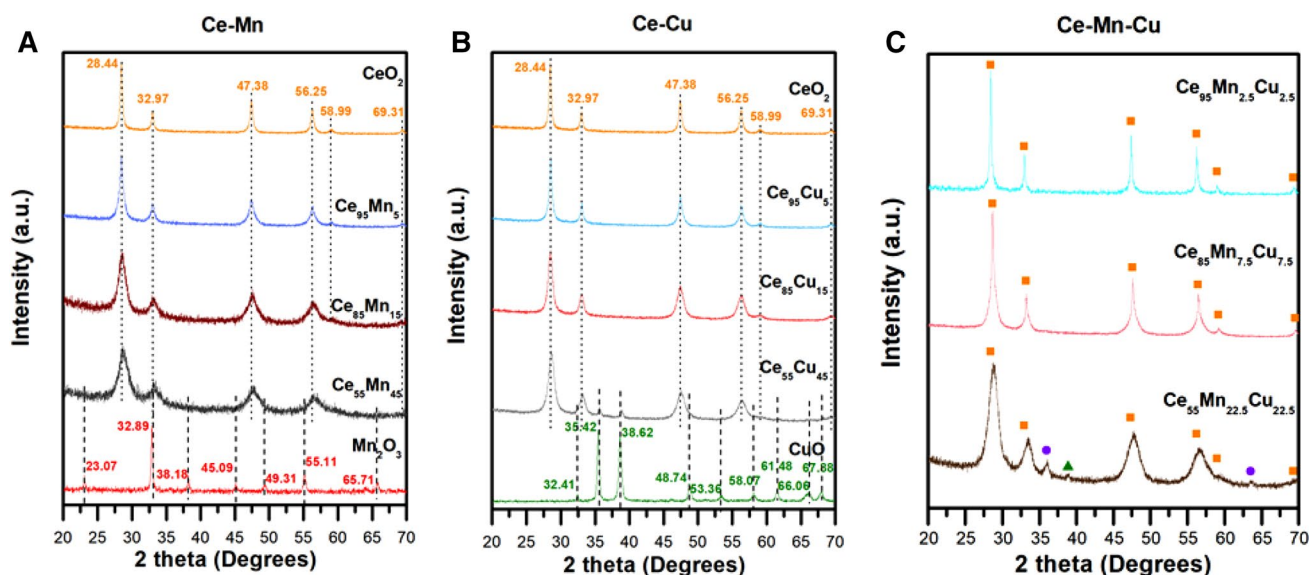

Fig. 1 XRD patterns for sets of samples: Ce–Mn (**a**), Ce–Cu (**b**) and Ce–Mn–Cu (**c**). Crystalline phases: CeO_2 = square; $Cu_{1.5}Mn_{1.5}O_4$ = circle; CuO = triangle

when foreign metals (= different radii) are introduced into the ceria framework.

Table 1 summarizes the various textural properties of the samples as derived from both XRD and N_2 physisorption analysis. As a whole, The BET surface areas were observed to have values in the range of 8–48 m^2 g^{-1}. Specifically, at lower foreign metal contents, the specific surface areas for mixed oxide samples increase with the Mn/Cu-loadings. On the other hand, at higher foreign metal contents worse textural properties can be observed. An exception to this trend occurs for the $Ce_{95}Mn_{2.5}Cu_{2.5}$ sample, exhibiting a smaller BET surface area (8 m^2 g^{-1}), probably due to the formation of big crystallites (Table 1; Fig. S1). Conversely, comparable pore volumes ($V_P = 0.02$–0.12 cm^3 g^{-1}) and pore diameters ($D_P = 11$–24 nm) can be observed for the prepared samples.

Figure 2 shows the morphological properties of the samples. Most of them exhibit a globular/sponge-like morphology, which is the feature of the parent oxide (CeO_2). In the case of Ce–Mn oxides, the size of such agglomerates seems to increase until the Mn content reaches 15 at.%. At higher Mn contents, the agglomerate size decreases. The previous behavior of the superficial features seems to follow the trend of the specific surface area reported in Table 1. The diameter of the globular agglomerates that constitute the Ce–Cu samples ($Ce_{95}Cu_5$ and $Ce_{85}Cu_{15}$) seems comparable, while $Ce_{55}Cu_{45}$ exhibits smaller spherical structures. Both the $Ce_{95}Mn_{2.5}Cu_{2.5}$ and $Ce_{85}Mn_{7.5}Cu_{7.5}$ samples show small agglomerates and compact structures with visible grain boundaries. Their predominantly non-porous structures confirm the low specific surface areas observed for the ternary oxide samples. The pure copper oxide sample (CuO) exhibits a compact structure with low porosity, while the pure manganese oxide (Mn_2O_3) demonstrates small pores distributed internally and externally on the surface. The EDS element maps of the catalysts containing 45% foreign metals are shown in Fig. S3. The analysis performed on some planar zones on the samples showed a uniform distribution of the elements on the catalytic surface. The atomic percentages obtained by the EDS analysis are shown in Table 2. The results show that the measured atomic percentages of the elements present in the sample are in fair agreement with the nominal percentages.

3.2 H_2-TPR and O_2-TPD Analysis

The H_2-TPR profiles of the synthesized catalysts are shown in Fig. 3. The reduction of CeO_2 started below 100 °C and was characterized by two main peaks: the one with a lower intensity at 194 °C and the one with a more remarkable intensity at 517 °C. According to the literature, the peak centered at higher temperature can be ascribed to the reduction of Ce species, while the peak appeared at lower temperatures corresponds to the reduction of surface oxygen species [19, 27]. Additionally, the signal occurring at higher temperature (above 600 °C) can be attributed to the reduction of cerium species in the bulk phase.

The reduction of copper oxide particles was characterized by one sharp peak centered at 266 °C, consistent with the literature [21, 28]. The reduction of Mn_2O_3 was characterized by two overlapping reduction peaks. The first one appeared at 325 °C and was attributed to the reduction step of $Mn_2O_3 \rightarrow Mn_3O_4$, and the second one was centered at 444 °C. The deconvolution of these two peaks revealed a total H_2 uptake of about 9.22 mmol g^{-1}, which is higher than the theoretical H_2 uptake of pure Mn_2O_3 (6.33 mmol g^{-1}). Such value is lower than the corresponding theoretical uptake when all the manganese is present in the Mn^{4+} form (11.50 mmol g^{-1}). This means that the aforementioned peaks correspond to the reduction of both Mn^{4+} and Mn^{3+} species, as evidenced by the XPS analysis. Therefore, the reduction pathway for the Mn_2O_3 sample, as reported in the literature, is $MnO_2 \rightarrow Mn_2O_3 \rightarrow Mn_3O_4 \rightarrow MnO$ [13, 29].

The H_2-TPR profiles of the binary Ce–Mn samples, as seen in Fig. 3a, show a multitude of overlapping reduction peaks at lower temperatures. In general, the H_2 uptake and catalyst reducibility increases with Mn-contents. The reduction profiles of the $Ce_{95}Mn_5$ and $Ce_{85}Mn_{15}$ catalysts show that the insertion of manganese into ceria lattice enhances the reducibility at lower temperatures, thus shifting the main reduction peak from 517 to 185 °C. In the case of $Ce_{55}Mn_{45}$, the reduction profile and the H_2 uptake change markedly and this can be due to the presence of manganese oxide species interacting with ceria.

Table 1 Textural properties of the samples as derived from the XRD and N_2 physisorption at −96 °C

Catalyst	Crystallite size[a] (nm)	S_{BET} (m^2 g^{-1})[b]	V_p (cm^3 g^{-1})[c]	D_p (nm)[d]
CeO_2	23	32	0.09	15
$Ce_{95}Mn_5$	12	39	0.07	11
$Ce_{85}Mn_{15}$	7	41	0.12	15
$Ce_{55}Mn_{45}$	4	21	0.11	17
$Ce_{95}Cu_5$	14	48	0.09	14
$Ce_{85}Cu_{15}$	10	26	0.08	22
$Ce_{55}Cu_{45}$	9	16	0.06	17
$Ce_{95}Mn_{2.5}Cu_{2.5}$	37	8	0.02	13
$Ce_{85}Mn_{7.5}Cu_{7.5}$	10	38	0.10	17
$Ce_{55}Mn_{22.5}Cu_{22.5}$	6	18	0.10	24
Mn_2O_3	44	15	0.11	28
CuO	27	1	0.01	18

[a]Calculated through the Scherrer formula

[b]Specific surface area calculated through the BET method

[c]Total pore volume

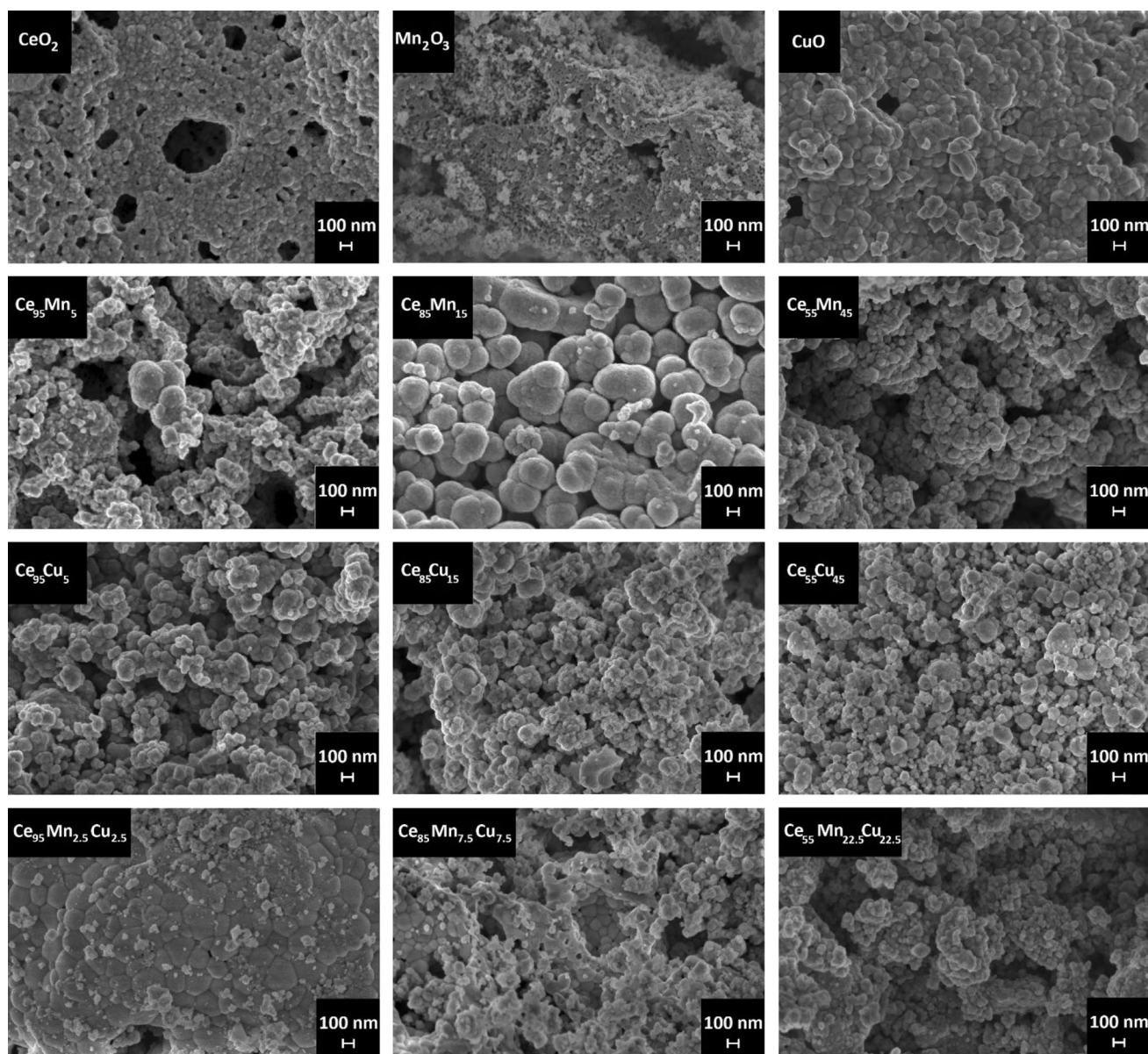[d]Pore diameter calculated according to the BJH method

Fig. 2 FESEM representative images of the fresh powder catalysts

Table 2 Chemical composition of the prepared samples (at.%) obtained from the EDS analysis

Sample	O (at.%)	Ce (at.%)	Cu (at.%)	Mn (at.%)
$Ce_{95}Mn_5$	67.00	31.20	–	1.80
$Ce_{85}Mn_{15}$	72.50	23.90	–	3.70
$Ce_{55}Mn_{45}$	69.80	18.10	–	12.10
$Ce_{95}Cu_5$	66.50	31.50	2.10	–
$Ce_{85}Cu_{15}$	62.00	31.50	6.50	–
$Ce_{55}Cu_{45}$	57.30	22.00	20.70	–
$Ce_{95}Mn_{2.5}Cu_{2.5}$	62.50	33.90	2.60	1.00
$Ce_{85}Mn_{7.5}Cu_{7.5}$	53.00	41.30	2.70	3.00
$Ce_{55}Mn_{22.5}Cu_{22.5}$	57.40	22.60	11.30	8.70

The reduction profiles of the Ce–Cu group of samples are shown in Fig. 3b. It can be noticed that the presence of Cu in the samples promotes the reducibility at lower temperatures. The $Ce_{95}Cu_5$ and $Ce_{85}Cu_{15}$ samples are characterized by two peaks, one appeared at 150 °C and another one at 169 °C (182 °C for the samples with higher copper contents). The peak at the lower temperature was attributed to Cu species in the lattice interacting with cerium (Ce–O–Cu), while the peak at the higher temperature can be assigned to highly dispersed CuO_x clusters interacting with ceria [19, 27, 28, 30]. For the $Ce_{55}Cu_{45}$ sample an additional peak appears at higher temperature, in which segregation of copper oxides and therefore further formation of crystalline CuO had

Fig. 3 H$_2$-TPR profiles of the Ce–Mn (**a**), Ce–Cu (**b**) and Ce–Mn–Cu (**c**) samples. Trends of the low-temperature reduction peaks for the prepared samples (**d**)
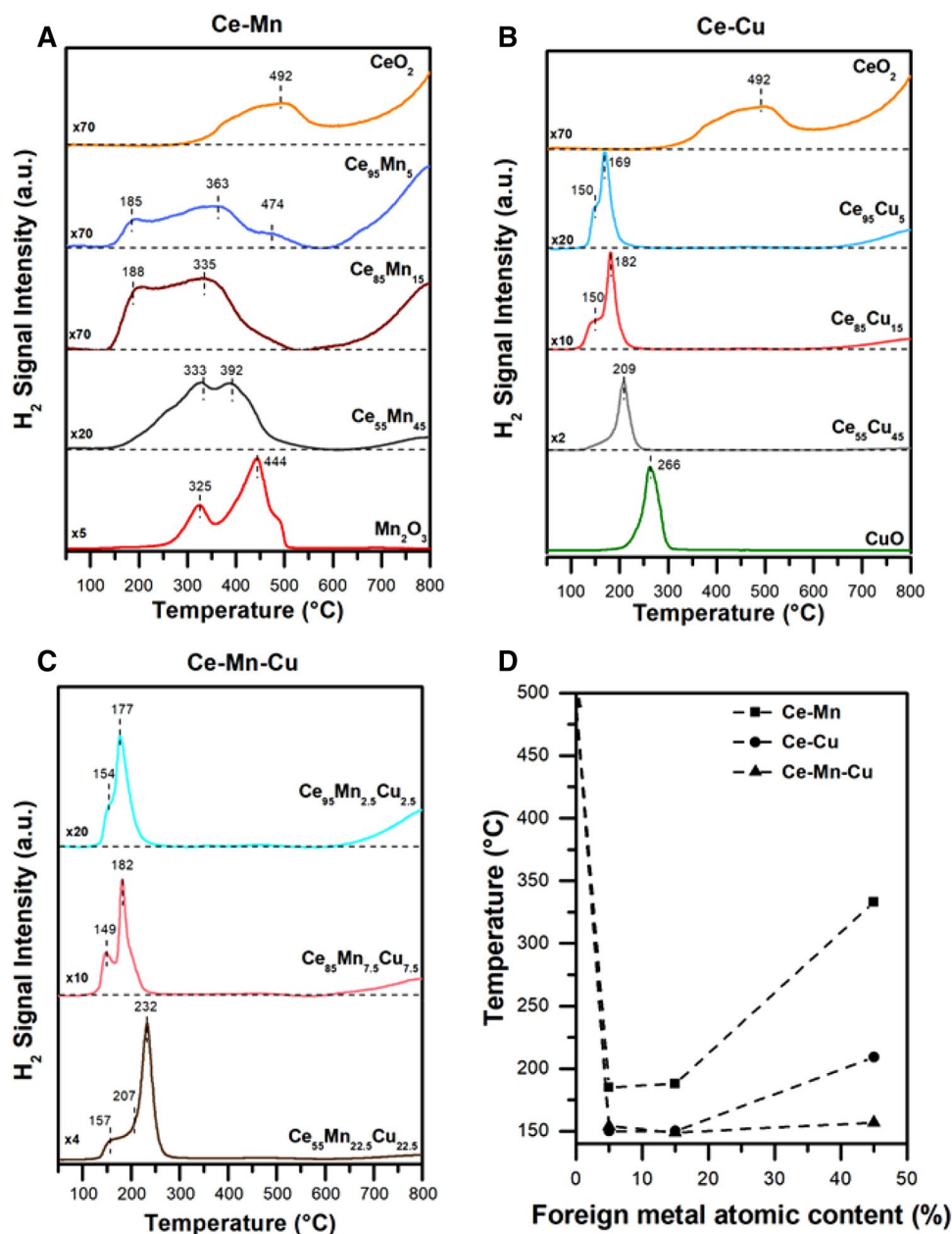
presumably occurred during the synthesis (as demonstrated by the XRD analysis). Therefore, the peak of Ce$_{55}$Cu$_{45}$ occurring at 209 °C is due to the reduction of CuO clusters dispersed on ceria [19, 27, 28, 30]. Finally, the surface reducibility of the Ce–Cu systems increases as a function of the Cu content, as follows: Ce$_{95}$Cu$_5$ < Ce$_{85}$Cu$_{15}$ < Ce$_{55}$Cu$_{45}$.

As seen in Fig. 3c, the reduction behavior of the Ce–Mn–Cu samples is similar to that of binary Ce–Cu samples, which generally exhibit two reduction peaks at about 150 °C and 180 °C. This means that the copper species gives the major contribution to the overall catalyst reducibility. However, the presence of manganese species in the ternary oxide samples seems to induce a slight shift of the reduction

peaks attributed to the copper species [31, 32]. The two reduction peaks of Ce$_{95}$Mn$_{2.5}$Cu$_{2.5}$ and Ce$_{85}$Mn$_{7.5}$Cu$_{7.5}$ were attributed to the reduction of isolated copper species interacting with cerium and manganese in the lattice (149 and 154 °C), and to the reduction of finely dispersed CuO$_x$ clusters interacting with the mixed oxide (177 and 182 °C). The H$_2$-TPR profile of the Ce$_{55}$Mn$_{22.5}$Cu$_{22.5}$ catalyst consists of several overlapping peaks, which in turn render more difficult the analysis of the reduction behavior. The peak at ca. 157 °C was attributed to the reduction of isolated copper species, which may be enhanced by the presence of manganese species. On the other hand, the signal at about 207 °C can be assigned to the combined reduction of the

$Cu_{1.5}Mn_{1.5}O_4$ spinel and the CuO_x clusters, both interacting with ceria. Finally, the peak centered at 232 °C was ascribed to the reduction of CuO species.

The trends of the low-temperature reduction peaks (Fig. 3d) show a possible role of the foreign metals in the ceria-based samples. It is evident that the presence of Mn/Cu species into the ceria shifts the reduction peaks at lower temperatures compared to pure ceria (= easier surface reducibility). Interestingly, for both the 5 and 15 at.% doped samples, the reduction peaks take place at the lowest temperature

Table 3 Hydrogen uptakes of the catalysts achieved during the H_2-TPR analysis and percentages of reduced Ce^{4+} species

Sample	H_2 uptake (mmol g_{cat}^{-1})	Red. Ce^{4+} (%)
CeO_2	0.61	20.9
$Ce_{95}Mn_5$	0.62	16.9[a]
$Ce_{85}Mn_{15}$	1.14	28.3[a]
$Ce_{55}Mn_{45}$	3.09	77.2[a]
$Ce_{95}Cu_5$	0.73	12.9[b]
$Ce_{85}Cu_{15}$	1.70	22.9[b]
$Ce_{55}Cu_{45}$	5.79	98.6[b]
$Ce_{95}Mn_{2.5}Cu_{2.5}$	0.61	4.7[c]
$Ce_{85}Mn_{7.5}Cu_{7.5}$	1.19	24.1[c]
$Ce_{55}Mn_{22.5}Cu_{22.5}$	3.96	56.6[c]
Mn_2O_3	9.22	–
CuO	17.34	–

[a] % of Ce^{4+} reduced if the initial oxidation state of Mn is +3

[b] % of Ce^{4+} reduced if the initial oxidation state of Cu is +2

[c] % of Ce^{4+} reduced if the initial oxidation state of Mn is +3 and for Cu is +2

(about 150 °C). This finding can be observed also in terms of H_2-uptake and may be related to the insertion of the metals in ceria's lattice with the formation of solid solutions. On the other hand, at higher metal contents the surface reduction occurs at higher temperatures, due to the presence of segregated Mn and Cu oxides as evidenced by the XRD data.

Finally, the deconvolution of the H_2-TPR profiles revealed the involvement of ceria during the reduction. Table 3 reports the total H_2 uptake of all the prepared catalysts and the percentage of Ce^{4+} species reduced during the analysis, on the assumption that the Mn and Cu species were initially present in the sample in the +3 and +2 oxidation states, respectively, and that they were reduced to Mn^{2+} and Cu^0. It can be seen that the overall H_2 uptake of the catalysts is generally higher than the stoichiometric uptake by the reduction of the manganese and/or copper species in the catalysts. In addition, the reduction of the Ce^{4+} species, which represents the participation of ceria in the reduction, seems to increase with foreign metal loading. This indicates a positive impact of both Mn and Cu as the foreign metals on improving the reducibility of ceria, possibly through the interactions among the oxides in the catalyst.

Figure 4 summarizes the results obtained from the O_2-TPD analysis. The O_2-TPD profiles of the binary Ce–Mn oxide samples are shown in Fig. 4a. The TPD profile of Mn_2O_3 shows one intense peak appeared at 826 °C. The estimated quantity of oxygen desorbed during the analysis, which corresponds to the peak integral area (1.09 mmol g^{-1}), matches the theoretical quantity of oxygen released in the reduction step $Mn_2O_3 \rightarrow Mn_3O_4$ (1.06 mmol g^{-1}). Similar value has also been reported elsewhere [13, 15]. The pure ceria sample (CeO_2) did not show any relevant oxygen
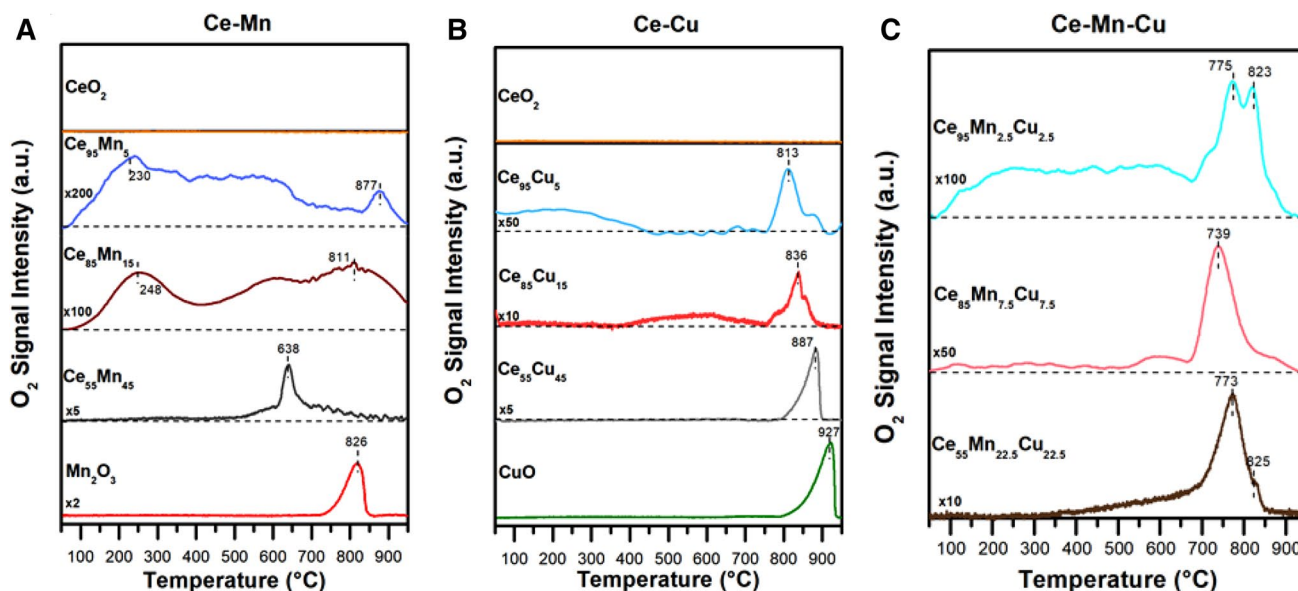

Fig. 4 O_2-TPD profiles of the Ce–Mn (**a**), Ce–Cu (**b**) and Ce–Mn–Cu (**c**) catalysts

desorption under the same analysis condition. To better analyze the oxygen desorption characteristics for the pure ceria sample, an additional analysis was performed under the conditions reported in the literature [33] and results are shown in Fig. S4. The peak appeared at approximately 850 °C, which corresponds to the desorption of superficial oxygen species. The presence of manganese in the Ce–Mn samples generally endorses an improvement in the catalyst oxygen storage capacity. According to the literature, the presence of Ce species in the solid promotes the higher oxidation state of Mn species at moderate temperatures [34]. The TPD profiles for the Ce–Mn–O_x samples show complex patterns (Fig. 4a). As a whole, the oxygen desorption at low temperatures (< 400 °C) can be attributed to the release of chemisorbed (O_α-type) species (magnification in Fig. S5), whereas the peaks at higher temperatures can be ascribed to lattice oxygen (O_β-type species) [35]. Specifically, the $Ce_{55}Mn_{45}$ sample demonstrates an intense peak centred at 638 °C, readily assigned to the reduction of Mn^{4+} species. On the other hand, different profiles can be observed for both $Ce_{85}Mn_{15}$ and $Ce_{95}Mn_5$ samples. For the latter samples, indeed, additional signals appear above 800 °C, thus suggesting the presence of reduced Mn^{3+}/Mn^{2+} species, along with Mn^{4+} cations. These results are in fair agreement with the XPS data (vide infra).

At lower temperature, the presence of multiple peaks suggests the presence of an abundant population of chemisorbed oxygen. These TPD results are in fair agreement with those derived from a set of commercial manganese oxides (MnO_2, Mn_2O_3 and MnO) included in Fig. S6: For the MnO_2 sample the reduction of Mn^{4+} to Mn^{3+} occurs at about 580 °C with an oxygen release of 2.63 mmol g^{-1} (step $MnO_2 \rightarrow Mn_2O_3$). This value is in fair agreement with the theoretical (calculated) oxygen release (2.87 mmol g^{-1}); the signal at higher temperature (ca. 811 °C) corresponds to the reduction of Mn^{3+} species to Mn^{2+}. The integral area of the latter peaks evidenced an oxygen release of 1.13 mmol g^{-1} (step $Mn_2O_3 \rightarrow Mn_3O_4$). The theoretical oxygen release for this step is about 1.06 mmol g^{-1}. Similar results occur with the reduction of Mn_2O_3 (peak at ca. 806 °C, oxygen release = 1.13 mmol g^{-1}) thus confirming that Mn^{3+} species can be reduced at about 800 °C. On the other hand, for the MnO sample there are not peaks in the TPD pattern, suggesting that Mn^{2+} species do not change their oxidation state during the analysis. Figure 4b also shows the O_2 desorption profiles for the CuO sample and the Ce–Cu catalysts. The reduction profile of CuO shows a single peak at 927 °C. The estimated quantity of oxygen desorbed during the analysis (3.13 mmol g^{-1}) is in accordance with the theoretical quantity of oxygen released in the reduction of Cu^{2+} to Cu^+ (3.14 mmol g^{-1}).

The TPD profiles for the Ce–Cu systems showed an enhancement of the O_α species when the percentage of copper was increased. Thus, the presence of Cu species improves the abundancy of chemisorbed oxygen species on CeO_2-based samples. Similarly, the O_β desorption rate seems to increase with the Cu content. The desorption peak of $Ce_{55}Cu_{45}$ is similar to that of pure CuO, although it is lower in intensity and centered at a lower temperature (*ca.* 887 °C). Such a similarity has led us to suggest that the desorption is probably related to the release of lattice oxygen of the CuO_x phases (i.e. $Cu^{2+} \rightarrow Cu^+$). Meanwhile, in the case of $Ce_{85}Cu_{15}$ and $Ce_{95}Cu_5$, the main desorption peaks are centered at slightly lower temperatures and are lower in intensity, most likely due to the decreasing amount of Cu^{2+} species. In addition, the wide peaks occurring between 400 and 700 °C were assigned to O_β released from the mixed Ce–O–Cu lattice.

Figure 4c shows that the co-presence of manganese and copper oxides in the ternary oxide samples enhances significantly the release of O_α-type species. The peaks centered at around 750 °C and 823 °C were ascribed to the release of O_β species. However, such ascription was not limited to weaker metal–oxygen bonds, since according to the O_2-TPD analysis of CeO_2 and Mn_2O_3, the peak ascribed to the weakening of Ce–O and Mn–O bonds was centered at a similar position. Moreover, as evidenced by the TPD profiles of the Ce–Cu samples, the desorption of Ce–O–Cu lattice oxygen may take place at a similar temperature.

3.3 X-ray Photoelectron Spectroscopy

Figure 5a shows the deconvoluted XPS spectra of the prepared samples in the O 1*s* core level. Three peaks that refer to various oxygen species were identified for most samples. The peak appeared in the binding energy (BE) range of 529.0–529.5 eV was attributed to the lattice-like oxygen species (O_β-species), which are bonded to Ce [36], while that appeared at 529.8 eV was attributed to the lattice-like oxygen species bonded to manganese or to copper [37, 38]. The peak between 531.1 eV and 531.5 eV was attributed to surface oxygen species (O_α-species) like O^-, or O_2^- and OH groups [39, 40]. The low-intensity peak appeared at higher BE range (between 533.2 and 534.3 eV) and it was observed in the spectra of the mixed oxide samples. This peak was attributed to the presence of more electrophilic O_α species like weakly adsorbed oxygen species [15, 41, 42]. As seen in Table 4, the O_α/O_β ratio for the Ce–Mn catalysts increases with Mn content, while that for copper-containing samples (i.e. Ce–Cu and Ce–Mn–Cu) seems to reach a minimum at the foreign metal content of 15 at%. For the mixed oxide samples, the abundance of O_α species is higher than that of CeO_2 but lower than those of Mn_2O_3 and CuO. The trend of the relative abundances of O_α among the mixed oxide catalysts observed via XPS analysis corroborates that of the oxygen release observed through the O_2-TPD analysis,

Fig. 5 XPS spectra of powder catalysts in the O (1s), Ce (3d), Mn (2p) and Cu (2p) core level regions
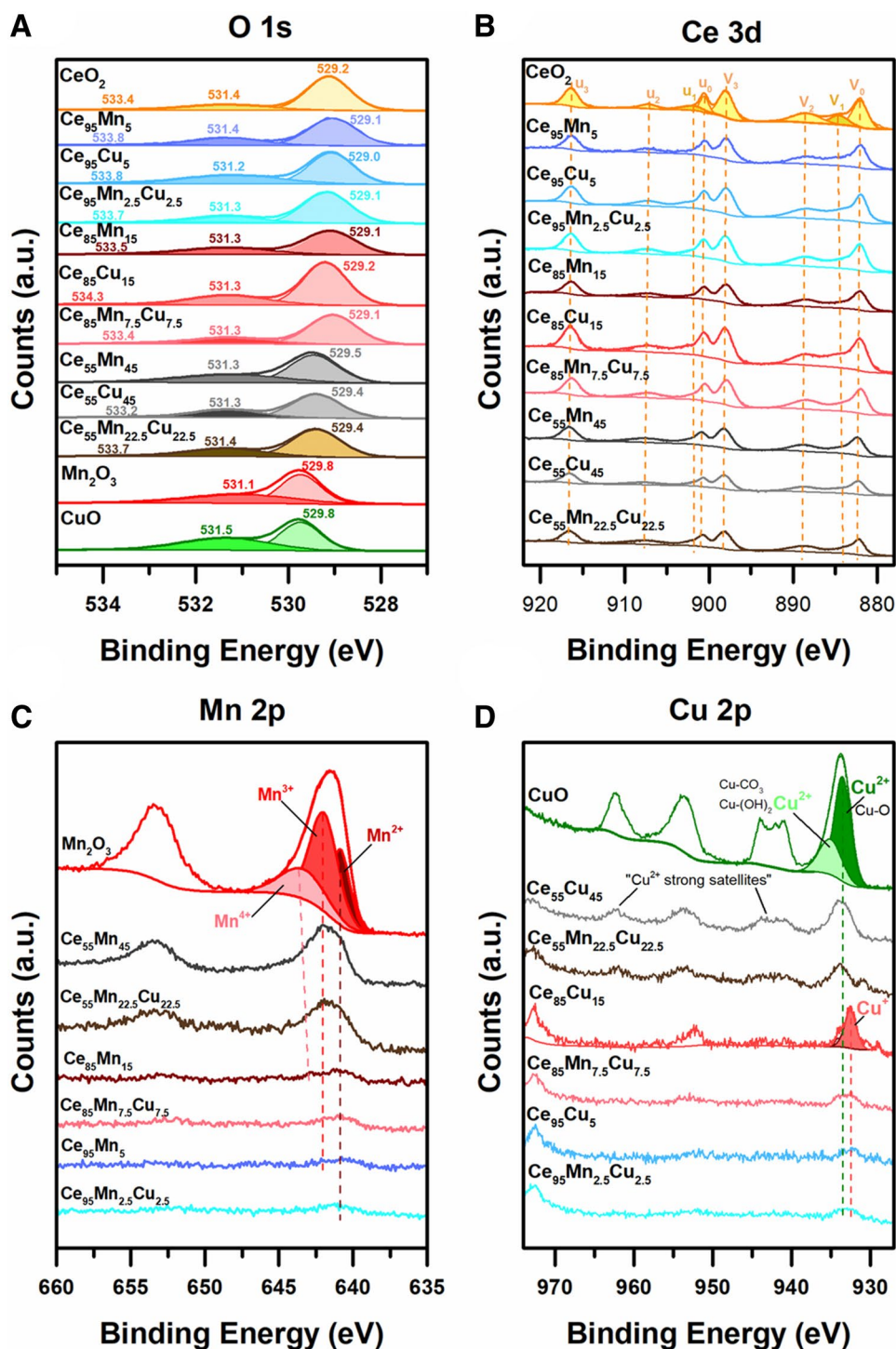
especially at low temperatures (< 400 °C), as shown in Fig. S5.

Figure 5b shows the Ce 3d XP spectra of all the ceria mixed oxides. Generally, the spectra are composed of a series of spin–orbit doublets "V" and "u", related to/located in the $3d_{5/2}$ and $3d_{3/2}$ regions, respectively. The common BE positions of such peaks, according to the current analysis, are as follows: V_0 at 882.0 eV; V_1 at 884.6 eV; V_2 at

888.4 eV; V_3 at 898.0 eV; and u_0 at 900.6 eV; u_1 at 902.0 eV; u_2 at 907.1 eV and u_3 at 916.3 eV. These peaks are related to cerium species with various oxidation states and were used to calculate the abundances of Ce^{4+} and Ce^{3+} on the surface. The doublets (V_0, u_0), (V_2, u_2) and (V_3, u_3) were assigned to Ce^{4+}, while the doublet (V_1, u_1) was assigned to Ce^{3+} [39, 43]. The relative abundances of these two species in the samples are summarized in Table 5. It can be seen that

Table 4 Oxygen species and their relative abundances (at.%) derived from the deconvolution of O 1s XPS spectra

Sample	O_α, OH BE (eV)	O_α (at.%)	O_β BE (eV)	O_β (at.%)	O_α/O_β
CeO_2	531.1; 533.6	26.2	529.2	73.8	0.35
$Ce_{95}Mn_5$	531.4; 533.8	30.9	529.1	69.1	0.45
$Ce_{85}Mn_{15}$	531.3; 533.5	33.0	529.1	66.0	0.50
$Ce_{55}Mn_{45}$	531.3	39.4	529.5	60.6	0.65
$Ce_{95}Cu_5$	531.2; 533.8	39.5	529	60.5	0.65
$Ce_{85}Cu_{15}$	531.3; 534.3	30.0	529.2	70.0	0.43
$Ce_{55}Cu_{45}$	531.3; 533.2	33.6	529.4	66.4	0.51
$Ce_{95}Mn_{2.5}Cu_{2.5}$	531.3; 533.7	29.3	529.1	70.7	0.41
$Ce_{85}Mn_{7.5}Cu_{7.5}$	531.3; 533.4	28.0	529.1	72.0	0.39
$Ce_{55}Mn_{22.5}Cu_{22.5}$	531.4; 533.7	33.0	529.4	67.0	0.49
Mn_2O_3	531.1	44.2	529.8	55.8	0.79
CuO	531.5	47.2	529.8	52.8	0.90

Table 5 Relative abundances (at.%) of cerium species derived from the deconvolution of Ce 3d XPS spectra

Sample	Ce^{4+} (at.%)	Ce^{3+} (at.%)	Ce^{4+}/Ce^{3+}
CeO_2	85.03	14.97	5.68
$Ce_{95}Mn_5$	71.96	28.04	2.57
$Ce_{85}Mn_{15}$	79.18	20.82	3.80
$Ce_{55}Mn_{45}$	78.78	21.22	3.71
$Ce_{95}Cu_5$	72.13	27.87	2.59
$Ce_{85}Cu_{15}$	74.08	25.92	2.86
$Ce_{55}Cu_{45}$	74.80	25.20	2.97
$Ce_{95}Mn_{2.5}Cu_{2.5}$	76.33	23.67	3.22
$Ce_{85}Mn_{7.5}Cu_{7.5}$	78.12	21.88	3.57
$Ce_{55}Mn_{22.5}Cu_{22.5}$	77.65	22.35	3.47

the atomic percentage of Ce^{3+} observed for the mixed oxide samples is higher than that of CeO_2. This indicates that the insertion of Mn and/or Cu in the ceria can produce a distortion in the fluorite framework. This leads to an increase in the abundancy of defects and therefore to the formation of new Ce^{3+} sites [39, 44, 45].

Figure 5c shows the Mn 2p XP spectra of the Mn-containing catalysts. The spin orbit peaks appeared in the range of 647.5–657.5 eV correspond to the $2p_{1/2}$ level, while those appeared between 638.5 and 647.5 eV correspond to the $2p_{3/2}$ level. The deconvolution of the $2p_{3/2}$ spectra has been used in many investigations to estimate the relative abundances of the Mn^{4+}, Mn^{3+} and Mn^{2+} species in the sample [13, 37]. The presence of these Mn species was observed for the Mn_2O_3 sample (Mn^{3+} are the most abundant ones). The relative amounts of Mn ions derived from the Mn 2p spectra deconvolution are summarized in Table S1. As a whole, it can be seen that the abundances of Mn species depend on the Mn content. In fact, the $Ce_{55}Mn_{45}$ sample has the highest amount of Mn^{4+} species among the samples, whereas for both

the binary ($Ce_{95}Mn_5$ and $Ce_{85}Mn_{15}$) and ternary oxides ($Ce_{95}Mn_{2.5}Cu_{2.5}$ and $Ce_{85}Mn_{7.5}Cu_{7.5}$), the abundancy of Mn^{2+} species is significantly higher.

Figure 5d finally shows the Cu 2p XP spectra of the copper-containing samples. The spin orbit peaks appeared in the range of 930.0–940.0 eV belong to the $2p_{3/2}$ level, whereas those in the range of 950.0–960.0 eV belong to the $2p_{1/2}$ level. The deconvolution of the latter is normally used to identify the copper species in the sample as well as the shake-ups related to those species [38, 46, 47]. In the case of the CuO, Cu^{2+} strong satellites at 942.5 and 962.5 eV were identified. Therefore, the major peak of $2p_{1/2}$ region was unarguably ascribed to Cu^{2+} and can be deconvoluted to two peak components: one centered at 933.6 eV and attributed to Cu species bonded to lattice oxygen (Cu–O), and another one centered at 935.2 eV and attributed to the copper hydroxide and/or copper carbonate species [38, 46]. The results for the deconvolution of the Cu 2p spectra are shown in Table S2. It can be observed that, in the case of $Ce_{55}Cu_{45}$ and $Ce_{55}Mn_{22.5}Cu_{22.5}$, the predominant oxidation state of Cu was + 2, most likely in the form of copper species bonded to lattice oxygen as well as to hydroxides/carbonates. The rest of the copper containing catalysts demonstrates a shift of the major $2p_{1/2}$ peak to a lower binding energy (932.5 eV), thus indicating the presence of Cu^+ species. Such a reduced species most likely originates from a reduction induced by an interaction among the metal cations [19, 38].

Finally, Table 6 shows the atomic percentages of the elements in the prepared samples. As a whole, it appears that XPS results are in fair agreement with EDS data (Table 2), thus suggesting a good dispersion of the foreign metals for both the surface and bulk phases. As shown in the new Table S3 (Supporting Information), the differences (in terms of ΔCu and ΔMn) between the two techniques are low and so it is not possible to argue any whole enrichment or diminution of the foreign metals on the sample surfaces with respect to the bulk compositions.

Table 6 Chemical composition of surface catalysts as analyzed by the XPS

Sample	O (at.%)	Ce (at.%)	Cu (at.%)	Mn (at.%)
$Ce_{95}Mn_5$	76.8	20.9	–	2.3
$Ce_{85}Mn_{15}$	80.7	15.6	–	3.6
$Ce_{55}Mn_{45}$	73.3	14.1	–	12.6
$Ce_{95}Cu_5$	75.2	19.4	5.4	–
$Ce_{85}Cu_{15}$	75.4	17.0	7.6	–
$Ce_{55}Cu_{45}$	73.8	11.2	15.0	–
$Ce_{95}Mn_{2.5}Cu_{2.5}$	77.6	13.4	5.3	3.7
$Ce_{85}Mn_{7.5}Cu_{7.5}$	75.5	19.5	2.0	3.1
$Ce_{55}Mn_{22.5}Cu_{22.5}$	69.2	11.3	12.4	7.0

3.4 Catalytic Activity of Powder Catalysts

3.4.1 Propylene Oxidation

As a whole, Fig. 6 shows the conversion of propylene (sections a, c and e) and ethylene (sections b, d and f) as a function of temperature for the prepared samples. The light-off temperature for the non-catalytic oxidation of propylene was observed at ca. 300 °C and the reaction reached a conversion of approximately 4% at 350 °C. In the presence of catalyst, the propylene oxidation reaction occurred at much lower temperatures and reached a complete conversion over several catalysts below 350 °C.

Table 7 summarizes the catalytic performances in terms of temperatures at which 10%, 50% and 90% propylene conversion to CO_2 are obtained ($T_{10\%}$, $T_{50\%}$ and $T_{90\%}$, respectively) as well as the reaction rates. Observing the $T_{10\%}$, $T_{50\%}$ and $T_{90\%}$ values, the performances for pure oxides follow this trend: CeO_2 (worst activity) $< CuO < Mn_2O_3$. The presence of foreign metals in the mixed oxides improves the performances in propylene oxidation, thus indicating possible interactions between Ce, Mn and/or Cu species or among different oxide phases on the surfaces (as revealed in the XRD analysis).

The substitution of Ce species with Mn/Cu atoms may enhance the oxygen defects in the samples, thus improving the mobility of lattice oxygen and consequently improving the reducibility of the samples, as evidenced by the TPR analysis. For each catalyst group, it was observed that both
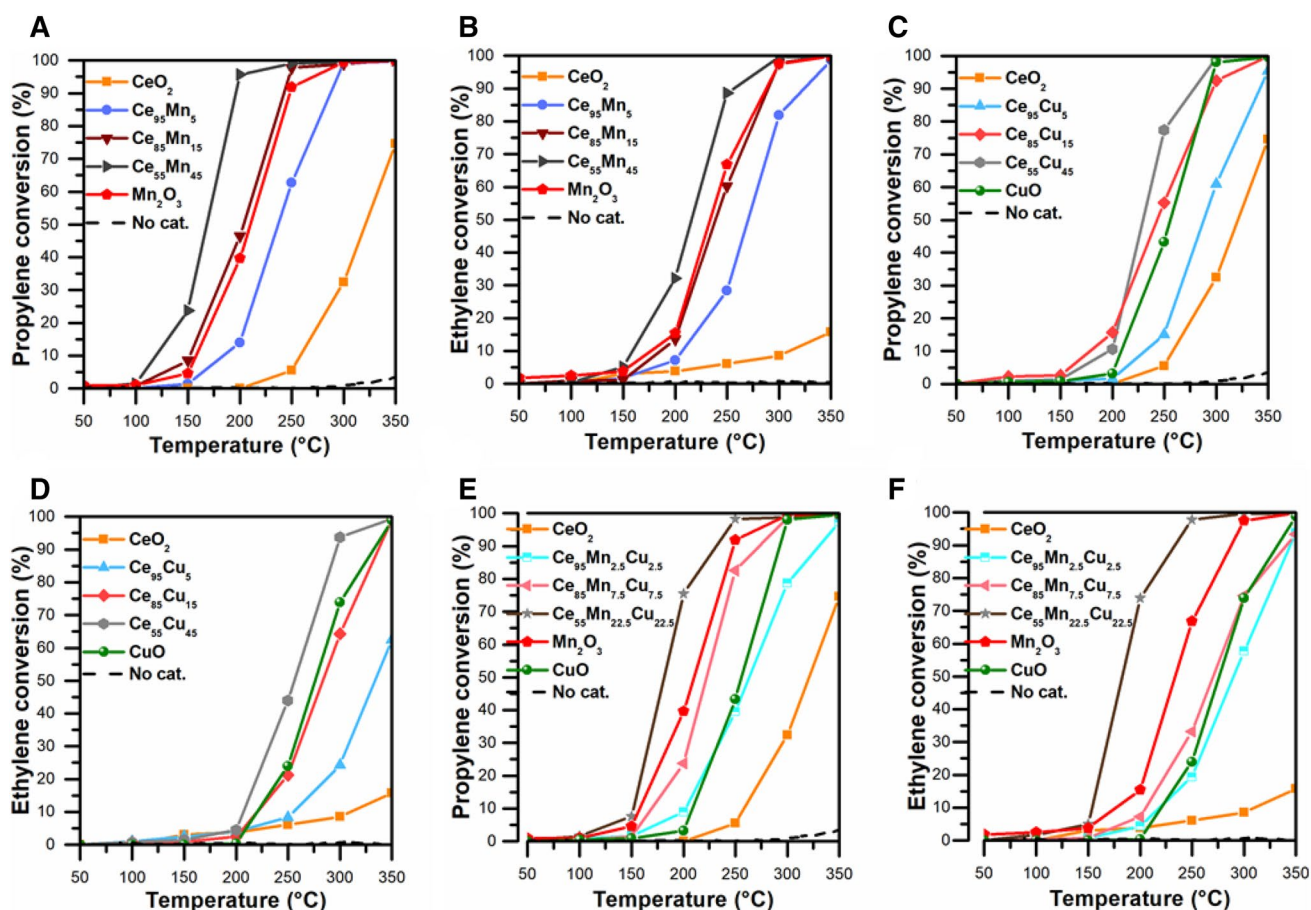

Fig. 6 Conversions (%) of propylene (**a**, **c**, **e**) and ethylene (**b**, **d**, **f**) over the prepared catalysts

Table 7 Catalytic performances of the prepared catalysts

Catalyst	Propylene oxidation				Ethylene oxidation			
	$T_{10\%}$ (°C)	$T_{50\%}$ (°C)	$T_{90\%}$ (°C)	r^a (µmol h^{-1} m^{-2})	$T_{10\%}$ (°C)	$T_{50\%}$ (°C)	$T_{90\%}$ (°C)	r^b (µmol h^{-1} m^{-2})
CeO_2	261	322	–	0.00	310	–	–	0.50
$Ce_{95}Mn_5$	193	237	283	0.11	210	270	313	0.32
$Ce_{85}Mn_{15}$	153	204	240	0.76	192	239	286	0.31
$Ce_{55}Mn_{45}$	130	168	194	3.54	163	216	252	1.21
$Ce_{95}Cu_5$	240	288	342	0.06	260	334	–	0.20
$Ce_{85}Cu_{15}$	186	243	295	0.34	227	283	337	0.26
$Ce_{55}Cu_{45}$	199	229	270	0.30	210	256	295	0.30
$Ce_{95}Mn_{2.5}Cu_{2.5}$	203	264	329	0.73	227	290	344	1.19
$Ce_{85}Mn_{7.5}Cu_{7.5}$	178	222	262	0.12	208	270	340	0.29
$Ce_{55}Mn_{22.5}Cu_{22.5}$	153	181	223	1.55	156	183	225	2.75
Mn_2O_3	161	210	248	1.26	190	233	283	1.09
CuO	212	257	290	3.04	227	276	330	1.10

[a]Reaction rates calculated at 150 °C

[b]Reaction rates calculated at 160 °C

catalytic performance and catalyst reducibility increased with metal loading, thus confirming the beneficial effect of metal cation substitution. On the other hand, the crystallite size, as evidenced by XRD analysis, decreased with metal loading. Interestingly, there is a good correlation between the performances of the mixed oxide catalysts and their crystal size: the lower the crystal sizes the better the performances (Fig. S7).

In terms of reaction rates (measured at 150 °C), mixed oxide catalysts generally exhibited better activities than CeO_2 and, in some cases, than Mn_2O_3 or CuO. The $Ce_{55}Mn_{45}$ sample, is the most intrinsically active catalysts and a complete propylene conversion over this catalyst can be achieved at 250 °C. Such a high performance is most likely derived from an interaction between MnO_x and CeO_x phases that further contributes to the improvement of redox properties of the catalyst. Then, a performance trend for the prepared systems can be drawn: Ce–Cu < Ce–Mn–Cu < Ce–Mn.

For the first time to our knowledge, these results confirm that the presence of Mn species into ceria-based catalysts prepared by SCS may promote the total oxidation of propylene.

Concerning the oxidation mechanism of propylene over metal oxide catalysts, many researchers argued that VOC molecules can be first adsorbed on the catalytic surface and then a symmetric allylic intermediate is formed as a consequence of the H-abstraction. Subsequently, the oxidation occurs on the catalyst surface by the release of lattice oxide (O^{2-}) and its consequent insertion in the chemical structure of the intermediate, thus forming an allyl alkoxide. Further H-abstraction takes place and the carbonyl bond leads to the formation of an aldehyde, which is then totally oxidized. Thus, the VOC oxidation over ceria-based catalysts seems to occur via a Mars–van Krevelen-type mechanism (Scheme 1) [19]. However, the presence of catalytic surfaces with abundant weakly-bonded oxygen species is beneficial for the oxidation process since organic molecules can be adsorbed and the reaction take place. Similarly, spillover phenomena may occur on the catalytic surface thus enhancing the whole reactivity [48–50].

Figure 7 (sections a, c and e) shows the results derived from the stability tests of the most active catalyst for each set (i.e. $Ce_{55}Cu_{45}$, $Ce_{55}Mn_{45}$ and $Ce_{55}Mn_{22.5}Cu_{22.5}$) in propylene oxidation. In all cases, reproducible results were achieved after three consecutive runs. In the case of $Ce_{55}Cu_{45}$, an early increase of CO_x at 150 °C can be related to a fast release of CO_2 at low temperature conditions. Moreover, the best catalyst ($Ce_{55}Mn_{45}$) was tested under the presence of humidity (RH 100%). Although worse catalytic performances were observed in the present case (Fig. S8), it appears that stable catalytic results can be observed for consecutive catalytic runs. This suggests that ceria-based catalysts acting in
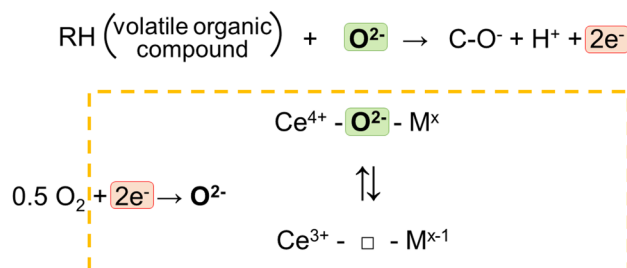
Scheme 1 Redox cycle of ceria-based systems (M″ and open square box represent the foreign metal, and the oxygen vacancy, respectively). Adapted from [19]
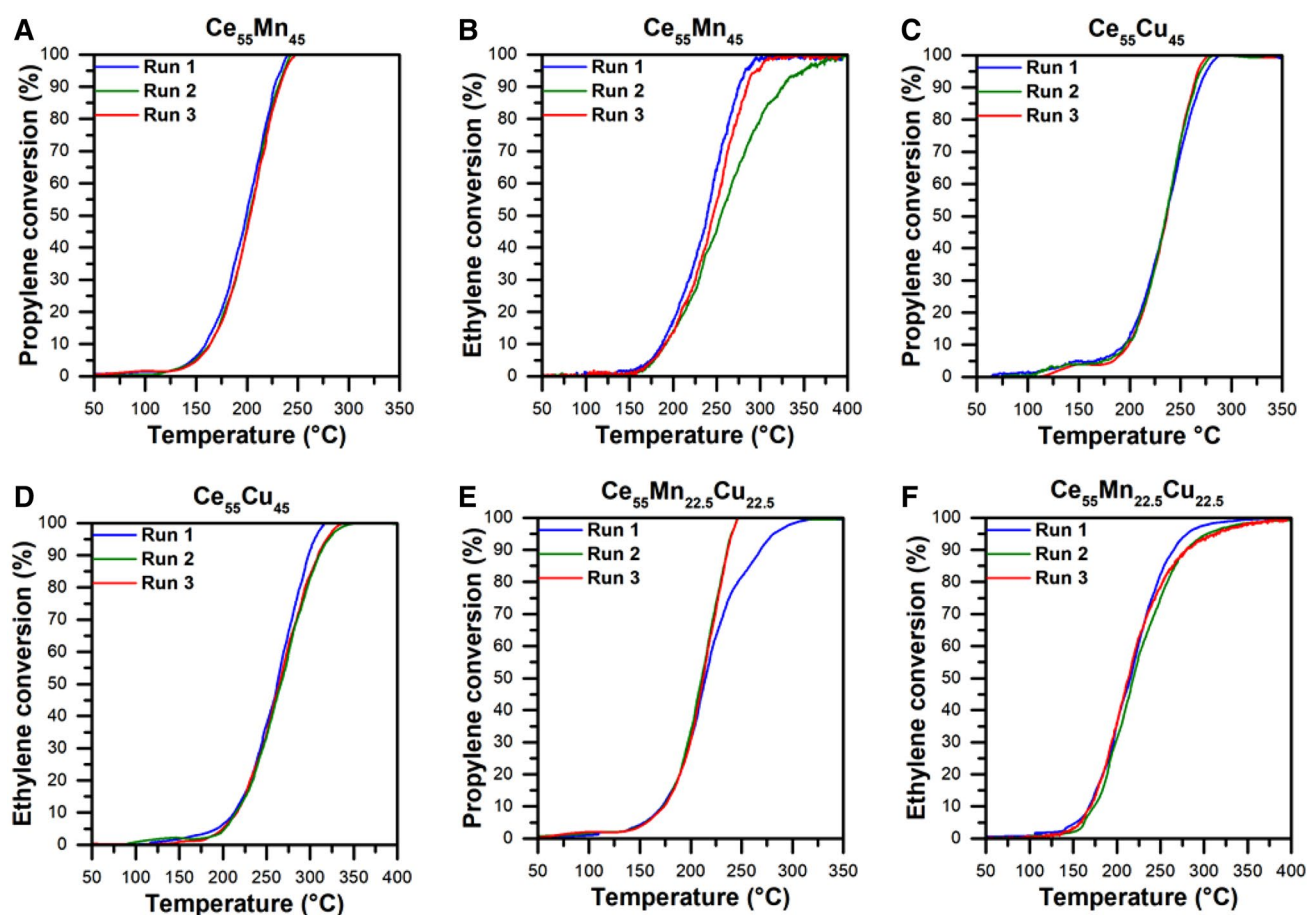
Fig. 7 Stability study performed in the oxidation of propylene (**a, c, e**) and ethylene (**b, d, f**) over the $Ce_{55}Mn_{45}$, $Ce_{55}Cu_{45}$ and $Ce_{55}Mn_{22.5}Cu_{22.5}$ catalysts

wet-conditions are less performing. This finding seems due to different causes, e.g. thermal phenomena localized on the catalytic particles, lower accessibility of active sites, etc.

Further kinetic experiments for the propylene oxidation over the $Ce_{55}Mn_{45}$ catalyst were performed varying the inlet VOC concentration (200, 400, 600 and 900 ppm) at 150 °C. As a whole, it was observed a positive (linear) dependence of the oxidation reaction rate (μmol_{VOC} h^{-1}) on the VOC concentration (Fig. S9.A).

3.4.2 Ethylene Oxidation

Figure 6 (sections b, d and f) shows the catalytic tests with ethylene oxidation. At 350 °C, the non-catalytic reaction reached < 1% ethylene conversion. In Table 7, it can be seen that the catalyzed ethylene oxidation also resulted in higher reaction temperatures than the catalyzed propylene oxidation and this demonstrates the lower ability of ethylene to be oxidized due to its higher stability. The catalytic performances for pure oxide samples (CeO_2, Mn_2O_3 and CuO) follow the same trend of the performances achieved in propylene

oxidation: $CeO_2 < CuO < M_2O_3$. The mixed oxide samples provided better performances than ceria and their catalytic activities increased with the foreign metal loadings, as well as for the propylene oxidation. Possible interactions between Ce, Mn and/or Cu species in the samples or among different phases are equally beneficial for ethylene oxidation.

As shown in Table 7, the $Ce_{55}Mn_{22.5}Cu_{22.5}$ sample is the most active catalyst for the ethylene oxidation at 160 °C followed by the $Ce_{55}Mn_{45}$ (2.75 and 1.21 μmol h^{-1} m^{-2}, respectively). Interestingly, the total conversion of ethylene over the $Ce_{55}Mn_{22.5}Cu_{22.5}$ sample was achieved at about 250 °C. These findings are possibly due to the interaction between the different active phases, as revealed on the $Ce_{55}Mn_{22.5}Cu_{22.5}$ sample (vide supra). For the first time to our knowledge, these results confirm that the presence of both Mn and Cu species into ceria-based catalysts prepared by SCS may promote the total oxidation of ethylene. Like in propylene oxidation and in many other VOC oxidations, ethylene oxidation may also be kinetically modelled via a redox-type cycle (i.e. Mars–van Krevelen reaction mechanism), which involves

the participation of surface oxygen species. Particularly in the case of ethylene, previous studies have shown that the oxidation mechanism involves a mild oxidation of the molecule on the surface of ceria and the formation of intermediate formate species, which are consequently oxidized to CO and CO_2 [51, 52].

A series of stability tests were equally performed with ethylene oxidation over the most active catalyst in each group (i.e. $Ce_{55}Cu_{45}$, $Ce_{55}Mn_{45}$ and $Ce_{55}Mn_{22.5}Cu_{22.5}$) and the results are shown in Fig. 7 (section b, d and f). After three consecutive runs, the complete ethylene conversion was achieved over powder catalysts at 350 °C.

As already mentioned for the propylene oxidation, the best catalyst ($Ce_{55}Mn_{22.5}Cu_{22.5}$) was tested under wet-conditions (Fig. S8). Although worse catalytic performances were observed at RH 100% rather than in dry conditions, comparable results were achieved for two consecutive catalytic runs in the presence of humidity. This further confirm the findings reported for the oxidation of propylene (vide supra).

Additionally, kinetic studies carried out over the $Ce_{55}Mn_{22.5}Cu_{22.5}$ sample with different inlet ethylene concentrations (200, 400, 600 and 900 ppm) at 160 °C confirm that the oxidation rate does not depend on VOC inlet concentration (Fig. S9.B), thus suggesting a zero order-type mechanism respect to the ethylene.

3.5 Catalytic Activity of the Catalyzed Monoliths

With the aim of evaluating the applicability of the most active catalysts studied in this work for industrial purposes, both the $Ce_{55}Mn_{45}$ and $Ce_{55}Mn_{22.5}Cu_{22.5}$ catalysts were deposited on SiC monoliths via in-situ synthesis. Figure 8 shows various FESEM images of a cross-sectional cut of an inner $Ce_{55}Mn_{22.5}Cu_{22.5}$–SiC channel taken at various magnifications. The images on the right were taken in back-scattered electron mode to better discriminate the catalytic washcoat (lighter color) from the SiC grains (darker color). The micrograph on the center shows the presence of catalytic washcoat on the inner wall of the monolith channel and confirms the effectiveness of the in situ synthesis in forming a thin catalytic layer (thickness of 326 nm in average) in the channel. Figure S3 (Section D) shows an EDS map that was performed on a representative zone of the sample. The map shows an even distribution of the elements over the surface.

Figure 9 (sections a and b) shows the stability tests with either propylene or ethylene oxidation over the $Ce_{55}Mn_{45}$–SiC monolith. In both reactions, the catalytic monolith is effective for the VOC oxidation. The catalytic reaction reached a complete propylene and ethylene conversion at around 500 °C and 600 °C, respectively, while the non-catalytic (thermal) oxidation is achieved at higher temperatures (ca. 670 °C). The catalyzed monolith also demonstrated comparable catalytic performances for three
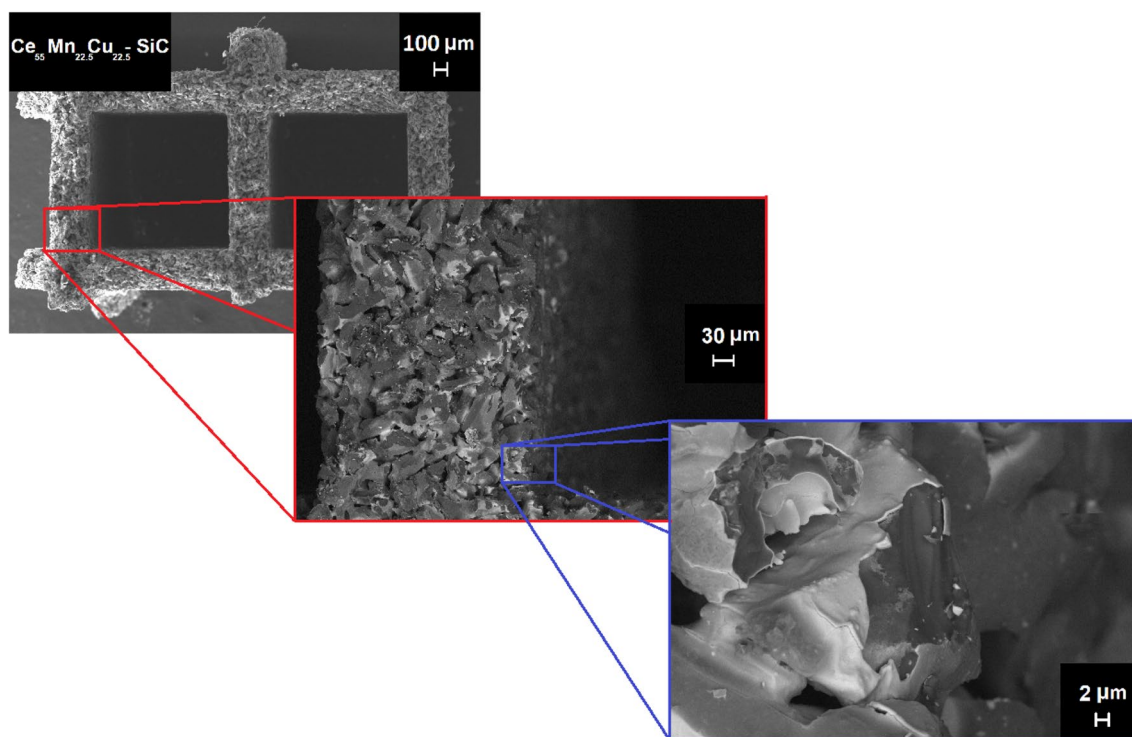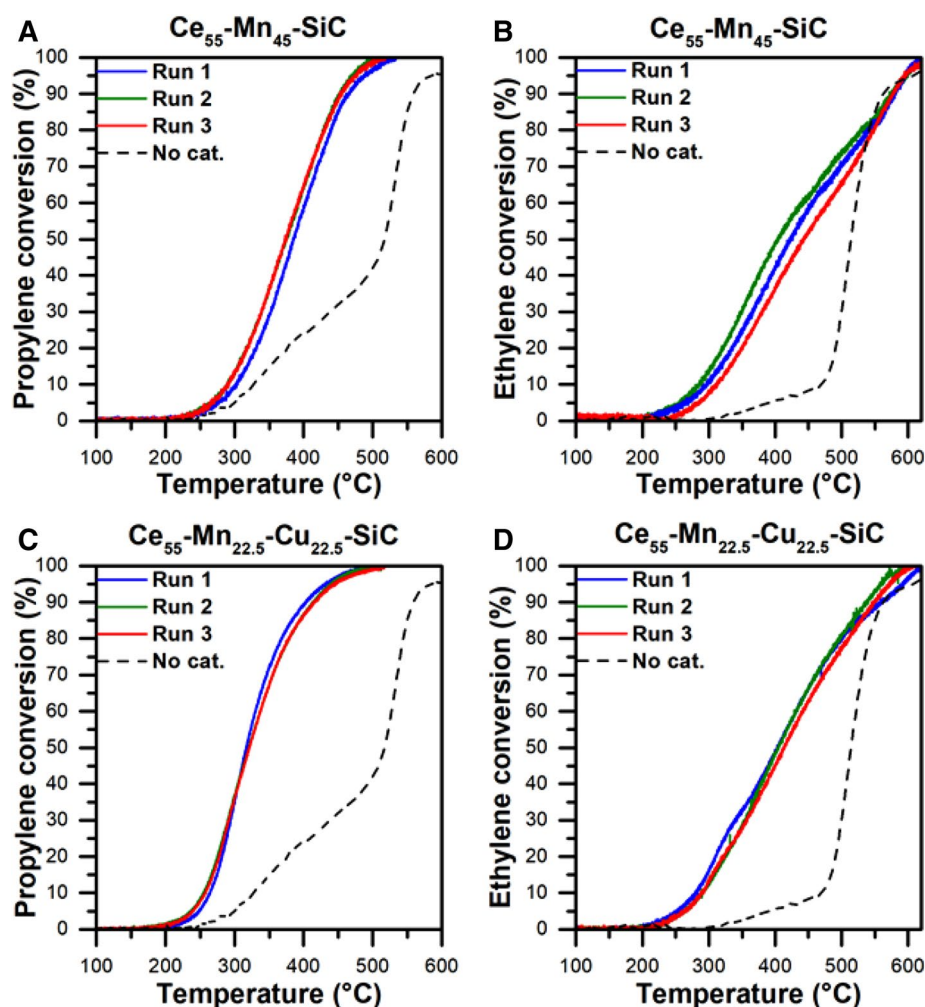

Fig. 8 FESEM images at different magnifications of the $Ce_{55}Mn_{22.5}Cu_{22.5}$–SiC monolith

Fig. 9 Conversions (%) of propylene (**a, c**) and ethylene (**b, d**) over Ce$_{55}$Mn$_{45}$–SiC and Ce$_{55}$Mn$_{22.5}$Cu$_{22.5}$–SiC monoliths

catalytic runs, thus confirming a good catalyst stability for both the oxidation reactions. To further verify the stability of Ce$_{55}$Mn$_{45}$–SiC, several time-on-stream (TOS) measurements were performed under two different isothermal conditions: (1) at higher temperature (470 and 590 °C for propylene and ethylene oxidation, respectively), at which a nearly complete VOC conversion was achieved and (2) at lower temperature (372 and 471 °C for propylene and ethylene oxidation, respectively), at which ca. 50% conversion can be achieved.

Similarly, Fig. 9 (sections c and d) shows the stability tests with either propylene or ethylene oxidation over the Ce$_{55}$Mn$_{22.5}$Cu$_{22.5}$–SiC monolith. As a whole, it was observed that the reaction mediated by Ce$_{55}$Mn$_{22.5}$Cu$_{22.5}$–SiC mostly occurred at lower temperatures than that mediated by Ce$_{55}$Mn$_{45}$–SiC. The catalyst stability was also appreciable after three consecutive runs.

A study of Ce$_{55}$Mn$_{45}$–SiC and Ce$_{55}$Mn$_{22.5}$Cu$_{22.5}$–SiC was carried out under two different isothermal conditions to investigate the stability at a nearly complete conversion and at 50% conversion. As shown in Fig. 10, fairly stable propylene/ethylene conversions can be observed over a TOS of 4 h,

thus suggesting promising structural and catalytic stability of the monoliths. A long term-stability study under isothermal conditions with the Ce$_{55}$Mn$_{22.5}$Cu$_{22.5}$–SiC has confirmed a stable catalytic behaviour for two catalytic runs over a time-on-stream of 12 h (Fig. S10).

In order to investigate the catalytic behavior of the monoliths under different operating conditions, additional experiments were done at various GHSV (namely, 1000, 4335, 9000 and 19,000 h^{-1}) as reported in Fig. 11. As a whole, a general trend occurs between the GHSV values and the catalytic performances for both the propylene and ethylene oxidation: the higher the GHSV the lower the VOC conversion. Specifically, the performances of the monolith-supported catalysts are closer to those of powder samples at 1000 h^{-1}, as a consequence of the higher residence time of the reactants into the channels. In fact, the worst results of catalyzed monoliths can be obtained at 19,000 h^{-1}. Finally, in order to evaluate the catalytic activity of the monoliths at the same W/F of powder catalysts, further experiments were conducted at 4335 h^{-1}. In the latter case, however, the performances of the monoliths are worse than those achieved

Fig. 10 Conversions (%) of propylene (**a**, **c**) and ethylene (**b**, **d**) over $Ce_{55}Mn_{45}$–SiC and $Ce_{55}Mn_{22.5}Cu_{22.5}$–SiC monoliths as a function of time-on-stream
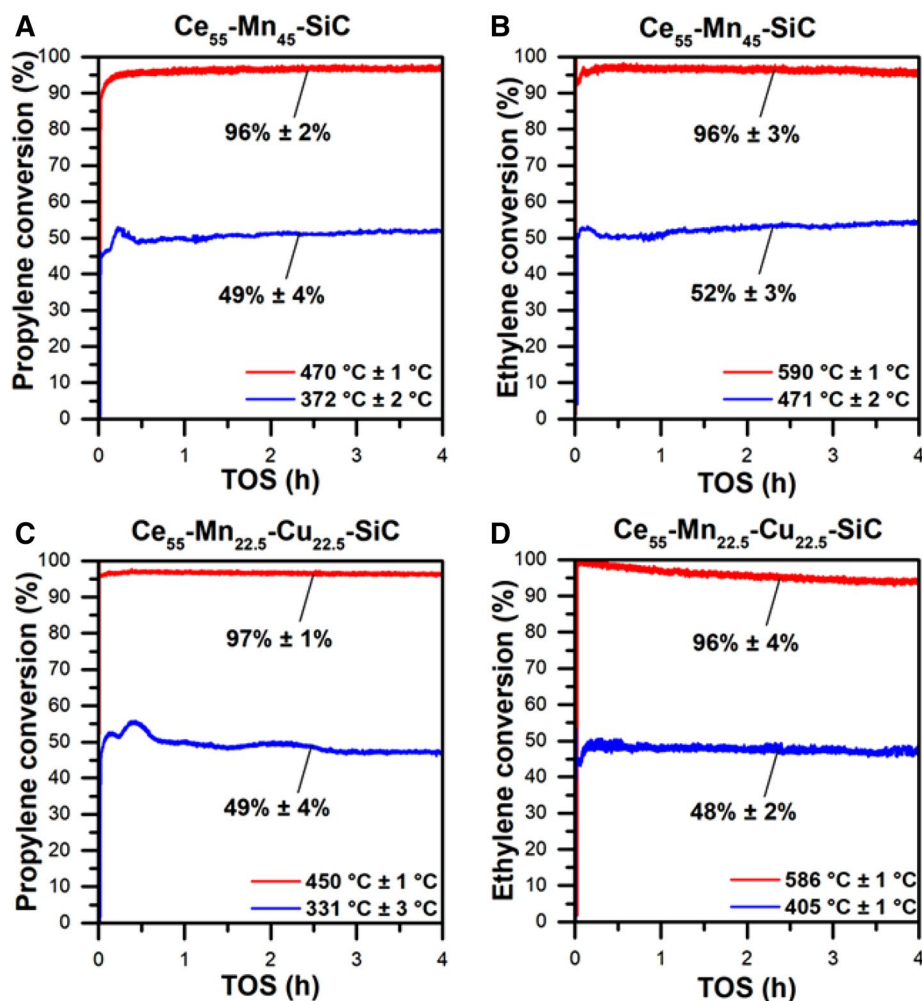
for powder catalysts (see Fig. 6). This finding suggests that both the different catalytic set-up and fluid dynamics play a key role on the whole activity [53, 54]. These findings suggest that it is possible to develop scaled-up catalytic systems (wash-coated monoliths) via a novel in-situ SCS, taking in consideration the chemical composition of powder catalysts.

4 Conclusions

In this work, several mixed oxide catalysts were synthesized via the solution combustion synthesis (SCS): two sets of binary oxides (Ce–Mn and Ce–Cu) and one set of ternary oxides (Ce–Mn–Cu), with various metal contents (5, 15 and 45 at.%). The results confirmed that the $Ce_{55}Mn_{45}$ was the most performing catalyst for total oxidation of propylene, thanks to possible interactions between MnO_x and CeO_x species. For total oxidation of ethylene, the ternary oxide $Ce_{55}Mn_{22.5}Cu_{22.5}$ was the most active catalyst, likely due to the interactions among CeO_x, $MnCuO_x$ and CuO_x species. In both cases, this catalytic improvement can be due to the enhanced reducibility of the catalysts.

Finally, two catalyzed monoliths ($Ce_{55}Mn_{45}$ and $Ce_{55}Mn_{22.5}Cu_{22.5}$) were prepared through a novel in-situ SCS and their performances were tested in a bench-scale reactor. The catalytic results confirmed stable performances in terms of VOC oxidation of either propylene or ethylene for a time-on stream of 4 h.

Fig. 11 Conversions (%) of propylene (**a**, **c**) and ethylene (**b**, **d**) on $Ce_{55}Mn_{45}$–SiC and $Ce_{55}Mn_{22.5}Cu_{22.5}$–SiC monoliths using four different GHSV

References

1. eCFR—Electronic Code of Federal Regulations Title 40—Chapter I—Subchapter C—Part 51—Subpart F. https://www.ecfr.gov/cgi-bin/text-idx?SID=9f2ffa73f1b399778c0c38af954be221&mc=true&node=sp40.2.51.f&rgn=div6. Accessed 3 May 2019
2. European Parliament and Council (2004) Directive 2004/42/CE on the limitation of emissions of volatile organic compounds due to the use of organic solvents in certain paints and varnishes and vehicle refinishing products and amending Directive 1999/13/EC. Off J Eur Union 10
3. Koppmann R (2007) Volatile organic compounds in the atmosphere. Blackwell Pub, Chicago
4. Bloemen HJT, Burn J (1993) Chemistry and analysis of volatile organic compounds in the environment. Springer, New York
5. Ramírez N, Cuadras A, Rovira E et al (2012) Chronic risk assessment of exposure to volatile organic compounds in the atmosphere near the largest Mediterranean industrial site. Environ Int 39:200–209. https://doi.org/10.1016/J.ENVINT.2011.11.002
6. Sarigiannis DA, Karakitsios SP, Gotti A et al (2011) Exposure to major volatile organic compounds and carbonyls in European indoor environments and associated health risk. Environ Int 37:743–765. https://doi.org/10.1016/J.ENVINT.2011.01.005
7. U.S. Environmental Protection Agency, Office of Air and Radiation (1992) Control techniques for volatile organic compound emissions from stationary sources
8. Moretti EC, American Institute of Chemical Engineers, Center for Waste Reduction Technologies. (2001) Practical solutions for reducing volatile organic compounds and hazardous air pollutants. Center for Waste Reduction Technologies, American Institute of Chemical Engineers
9. Kamal MS, Razzak SA, Hossain MM (2016) Catalytic oxidation of volatile organic compounds (VOCs)—a review. Atmos

Environ 140:117–134. https://doi.org/10.1016/J.ATMOS ENV.2016.05.031

10. Spivey JJ (1987) Complete catalytic oxidation of volatile organics. Ind Eng Chem Res 26:2165–2180. https://doi.org/10.1021/ie00071a001

11. Fino D, Bensaid S, Piumetti M, Russo N (2016) A review on the catalytic combustion of soot in Diesel particulate filters for automotive applications: From powder catalysts to structured reactors. Appl Catal A Gen 509:75–96. https://doi.org/10.1016/J.APCATA.2015.10.016

12. Zhang Z, Jiang Z, Shangguan W (2016) Low-temperature catalysis for VOCs removal in technology and application: a state-of-the-art review. Catal Today 264:270–278. https://doi.org/10.1016/j.cattod.2015.10.040

13. Piumetti M, Fino D, Russo N (2015) Mesoporous manganese oxides prepared by solution combustion synthesis as catalysts for the total oxidation of VOCs. Appl Catal B Environ 163:277–287. https://doi.org/10.1016/j.apcatb.2014.08.012

14. Kim SC, Shim WG (2010) Catalytic combustion of VOCs over a series of manganese oxide catalysts. Appl Catal B Environ 98:180–185. https://doi.org/10.1016/j.apcatb.2010.05.027

15. Santos VP, Pereira MFR, Órfão JJM, Figueiredo JL (2010) The role of lattice oxygen on the activity of manganese oxides towards the oxidation of volatile organic compounds. Appl Catal B Environ 99:353–363. https://doi.org/10.1016/j.apcatb.2010.07.007

16. Heynderickx PM, Thybaut JW, Poelman H et al (2010) The total oxidation of propane over supported Cu and Ce oxides: a comparison of single and binary metal oxides. J Catal 272:109–120. https://doi.org/10.1016/j.jcat.2010.03.006

17. Trovarelli A (2002) Catalysis by ceria and related materials. Imperial College Press, London

18. Ruiz Puigdollers A, Schlexer P, Tosoni S, Pacchioni G (2017) Increasing oxide reducibility: the role of metal/oxide interfaces in the formation of oxygen vacancies. ACS Catal 7:6493–6513. https://doi.org/10.1021/acscatal.7b01913

19. Piumetti M, Bensaid S, Andana T et al (2017) Cerium–copper oxides prepared by solution combustion synthesis for total oxidation reactions: From powder catalysts to structured reactors. Appl Catal B Environ 205:455–468. https://doi.org/10.1016/j.apcatb.2016.12.054

20. Delimaris D, Ioannides T (2008) VOC oxidation over MnO$_x$–CeO$_2$ catalysts prepared by a combustion method. Appl Catal B Environ 84:303–312. https://doi.org/10.1016/j.apcatb.2009.02.003

21. Delimaris D, Ioannides T (2009) VOC oxidation over CuO–CeO$_2$ catalysts prepared by a combustion method. Appl Catal B Environ 89:295–302. https://doi.org/10.1016/j.apcatb.2009.02.003

22. Lu H, Kong X, Huang H et al (2015) Cu–Mn–Ce ternary mixed-oxide catalysts for catalytic combustion of toluene. J Environ Sci 32:102–107. https://doi.org/10.1016/J.JES.2014.11.015

23. Yu P, Zhang X, Chen Y, Ma Y (2010) Solution-combustion synthesis of ε-MnO$_2$ for supercapacitors. Mater Lett 64:61–64. https://doi.org/10.1016/J.MATLET.2009.10.007

24. González-Cortés SL, Imbert FE (2013) Fundamentals, properties and applications of solid catalysts prepared by solution combustion synthesis (SCS). Appl Catal A Gen 452:117–131. https://doi.org/10.1016/J.APCATA.2012.11.024

25. Papavasiliou J, Avgouropoulos G, Ioannides T (2006) In situ combustion synthesis of structured Cu–Ce–O and Cu–Mn–O catalysts for the production and purification of hydrogen. Appl Catal B Environ 66:168–174. https://doi.org/10.1016/J.APCATB.2006.03.011

26. Ertl G, Knoezinger H, Schueth F, Weitkamp J (2008) Handbook of heterogeneous catalysis. Wiley, Weinheim

27. Guo X, Zhou R (2016) A new insight into the morphology effect of ceria on CuO/CeO$_2$ catalysts for CO selective oxidation in hydrogen-rich gas. Catal Sci Technol 6:3862–3871. https://doi.org/10.1039/c5cy01816a

28. Avgouropoulos G, Ioannides T (2003) Selective CO oxidation over CuO–CeO$_2$ catalysts prepared via the urea–nitrate combustion method. Appl Catal A Gen 244:155–167. https://doi.org/10.1016/S0926-860X(02)00558-6

29. Kapteijn F, Singoredjo L, Andreini A, Moulijn JA (1994) Activity and selectivity of pure manganese oxides in the selective catalytic reduction of nitric oxide with ammonia. Appl Catal B Environ 3:173–189. https://doi.org/10.1016/0926-3373(93)E0034-9

30. Li Y, Fu Q, Flytzani-Stephanopoulos M (2000) Low-temperature water-gas shift reaction over Cu- and Ni-loaded cerium oxide catalysts. Appl Catal B Environ 27:179–191. https://doi.org/10.1016/S0926-3373(00)00147-8

31. Wang H, Lu Y, Han YX et al (2017) Enhanced catalytic toluene oxidation by interaction between copper oxide and manganese oxide in Cu–O–Mn/γ-Al$_2$O$_3$ catalysts. Appl Surf Sci 420:260–266. https://doi.org/10.1016/j.apsusc.2017.05.133

32. Wöllner A, Lange F, Schmelz H, Knözinger H (1993) Characterization of mixed copper-manganese oxides supported on titania catalysts for selective oxidation of ammonia. Appl Catal A Gen 94:181–203. https://doi.org/10.1016/0926-860X(93)85007-C

33. Palmisano P, Russo N, Fino P et al (2006) High catalytic activity of SCS-synthesized ceria towards diesel soot combustion. Appl Catal B Environ 69:85–92. https://doi.org/10.1016/J.APCATB.2006.06.002

34. Imamura S, Shono M, Okamoto N et al (1996) Effect of cerium on the mobility of oxygen on manganese oxides. Appl Catal A Gen 142:279–288. https://doi.org/10.1016/0926-860X(96)00095-6

35. Liang Q, Wu X, Weng D, Xu H (2008) Oxygen activation on Cu/Mn-Ce mixed oxides and the role in diesel soot oxidation. Catal Today 139:113–118. https://doi.org/10.1016/j.cattod.2008.08.013

36. Platau A, Johansson LI, Hagström AL et al (1977) Oxidation of cerium and titanium studied by photoelectron spectroscopy. Surf Sci 63:153–161. https://doi.org/10.1016/0039-6028(77)90334-X

37. Biesinger MC, Payne BP, Grosvenor AP et al (2011) Resolving surface chemical states in XPS analysis of first row transition metals, oxides and hydroxides: Cr, Mn, Fe, Co and Ni. Appl Surf Sci 257:2717–2730. https://doi.org/10.1016/j.apsusc.2010.10.051

38. Biesinger MC, Lau LWM, Gerson AR, Smart RSC (2010) Resolving surface chemical states in XPS analysis of first row transition metals, oxides and hydroxides: Sc, Ti, V, Cu and Zn. Appl Surf Sci 257:887–898. https://doi.org/10.1016/j.apsusc.2010.10.051

39. Chen D, He D, Lu J et al (2017) Investigation of the role of surface lattice oxygen and bulk lattice oxygen migration of cerium-based oxygen carriers: XPS and designed H2-TPR characterization. Appl Catal B Environ 218:249–259. https://doi.org/10.1016/j.apcatb.2017.06.053

40. Dupin J-C, Gonbeau D, Vinatier P, Levasseur A (2000) Systematic XPS studies of metal oxides, hydroxides and peroxides. Phys Chem Chem Phys 2:1319–1324. https://doi.org/10.1039/A908800H

41. Deng W, Dai Q, Lao Y et al (2015) Low temperature catalytic combustion of 1,2-dichlorobenzene over CeO$_2$–TiO$_2$ mixed oxide catalysts. Appl Catal B Environ 181:848–861. https://doi.org/10.1016/j.apcatb.2015.07.053

42. Lin X, Li S, He H et al (2018) Evolution of oxygen vacancies in MnO$_x$–CeO$_2$ mixed oxides for soot oxidation. Appl Catal B Environ 223:91–102. https://doi.org/10.1016/j.apcatb.2017.06.071

43. Mullins DR (2015) The surface chemistry of cerium oxide. Surf Sci Rep 70:42–85. https://doi.org/10.1016/j.surfrep.2014.12.001

44. Machida M, Uto M, Kurogi D, Kijima T (2000) MnO(x)–CeO$_2$ binary oxides for catalytic NO(x) sorption at low temperatures. Sorptive removal of NO(x). Chem Mater 12:3158–3164. https://doi.org/10.1021/cm000207r

45. Dosa M, Piumetti M, Bensaid S et al (2018) Novel Mn–Cu-containing CeO_2 nanopolyhedra for the oxidation of CO and diesel soot: effect of dopants on the nanostructure and catalytic activity. Catal Lett 148:298–311. https://doi.org/10.1007/s10562-017-2226-y

46. Kundakovic L, Flytzani-Stephanopoulos M (1998) Reduction characteristics of copper oxide in cerium and zirconium oxide systems. Appl Catal A Gen 171:13–29. https://doi.org/10.1016/S0926-860X(98)00056-8

47. Liu W, Flytzani-Stephanopoulos M (1995) Total oxidation of carbon monoxide and methane over transition metal-fluorite oxide composite catalysts. J Catal 153:317–332

48. Reitz JB, Solomon EI (1998) Propylene oxidation on copper oxide surfaces: Electronic and geometric contributions to reactivity and selectivity. J Am Chem Soc 120:11467–11478. https://doi.org/10.1021/ja981579s

49. Wood BJ, Wise H, Yolles RS (1969) Selectivity and stoichiometry of copper oxide in propylene oxidation. J Catal 15:355–362. https://doi.org/10.1016/0021-9517(69)90304-2

50. Santos VP, Pereira MFR, Órfão JJM, Figueiredo JL (2009) Synthesis and characterization of manganese oxide catalysts for the total oxidation of ethyl acetate. Top Catal 52:470–481. https://doi.org/10.1007/s11244-009-9187-3

51. Li C, Xin Q, Guo X (1992) Surface oxygen species and their reactivities in the mild oxidation of ethylene on cerium oxide studied by FT-IR spectroscopy. Catal Lett 12:297–305. https://doi.org/10.1007/BF00767212

52. Njagi EC, Genuino HC, King'Ondu CK et al (2012) Catalytic oxidation of ethylene at low temperatures using porous copper manganese oxides. Appl Catal A Gen 421–422:154–160. https://doi.org/10.1016/j.apcata.2012.02.011

53. Zhang X, Wu D (2016) Ceramic monolith supported Mn–Ce–M ternary mixed-oxide (M = Cu, Ni or Co) catalyst for VOCs catalytic oxidation. Ceram Int 42:16563–16570. https://doi.org/10.1016/J.CERAMINT.2016.07.076

54. Morales MR, Yeste MP, Vidal H et al (2017) Insights on the combustion mechanism of ethanol and n-hexane in honeycomb monolithic type catalysts: Influence of the amount and nature of Mn–Cu mixed oxide. Fuel 208:637–646. https://doi.org/10.1016/J.FUEL.2017.07.069

Affiliations

Miguel Jose Marin Figueredo[1] · Tahrizi Andana[1] · Samir Bensaid[1] · Melodj Dosa[1] · Debora Fino[1] · Nunzio Russo[1] · Marco Piumetti[1]

✉ Marco Piumetti
marco.piumetti@polito.it

Miguel Jose Marin Figueredo
miguel.marinfigueredo@polito.it

Tahrizi Andana
tahrizi.andana@polito.it

Samir Bensaid
samir.bensaid@polito.it

Melodj Dosa
melodj.dosa@polito.it

Debora Fino
debora.fino@polito.it

Nunzio Russo
nunzio.russo@polito.it

[1]   Department of Applied Science and Technology, Politecnico Di Torino, Corso Duca degli Abruzzi 24, 10129 Torino, Italy